iFlpMosaics: A method for the ratiometric induction and high-throughput comparative analysis of mutant and wildtype cells

Irene Garcia-Gonzalez[1], Stefano Gambera[1], Alvaro Regano[1], Susana F. Rocha[1], Lourdes Garcia-Ortega[1], Mariya Lytvyn[1], Maria S. Sanchez-Muñoz[1], Aroa Garcia-Cabero[1], Ivana Zagorac[1], Wen Luo[1], Macarena Fernández-Chacón[1], Verónica Casquero-Garcia[1], Federica Francesca Lunella[1], Rui Benedito[1].*

1-Molecular Genetics of Angiogenesis Group, Centro Nacional de Investigaciones Cardiovasculares (CNIC), Madrid, Spain.

* Corresponding author. Rui.Benedito@cnic.es

In order to understand gene function, cells mutated for a gene need to be compared with normal cells. In most biomedical studies this comparative analysis is carried out with cells present in different animals and therefore not experiencing the same microenvironment or epigenetic changes. Here, we present a large set of new genetic tools and mouse lines that enable Flp recombinase-dependent ratiometric induction and single-cell clonal tracking of multiple fluorescently labeled normal and Cre-mutant cells from either distinct or the same progenitor cells. The labelled cells can be profiled *in situ* by multispectral imaging, or by FACS and scRNA-seq. With these new tools, normal and mutant cells can be ratiometrically induced and multispectrally barcoded within the same temporal window and tissue microenvironment. This enables a better understanding of how induced genetic mutations affect the biology of single cells with higher accuracy and reliability during tissue development, homeostasis, or disease.

Introduction

When a gene is deleted or mutated in a cell, it generates a cascade of events that may result in a significant change in its phenotype, as well as that of the surrounding tissue over time. Often scientists analyse mutant cells or tissues that carry genetic mutations for several days, weeks, months or even years and compare their phenotype with independent control cells or tissues of distinct non-mutant (control) animals. During the process of gene mutation to phenotypic manifestation or analysis, often the targeted and surrounding tissue biology changes significantly, which may interact with and change the final phenotype of the mutant cells. An example of this, is the conditional deletion or activation of genes important for vascular, neuronal or cancer development. Mutations that impact tissue function or development, frequently result in a change of the surrounding tissues. Since the non-targeted tissues that surround mutant cells are themselves the source of many biochemical factors, their abnormal

development or function results in the change of a key feedback mechanism that impacts the phenotype of the mutant cells, in a non-cell-autonomous manner, and independently of the initially induced genetic mutation itself (Hansen and Hippenmeyer, 2020; Hansen et al., 2022). This often generates secondary mutant tissue phenotypes over time, that may confound the interpretation of the real or primary gene function on a mutant cell phenotype.

Genetic mosaics are a particularly powerful research tool to overcome these problems because they allow the study of genetic cell-autonomous effects when distinct mutant and control (wildtype) cells arise from the same progenitor cells, and confront the same microenvironment, in the same tissue or organism. In this case, the only difference between the cells used for comparative analysis is the induced mutation in an otherwise identical organism, genetic background and tissue microenvironment.

Mouse models that allow the timed-induction of somatic genetic mosaics are therefore essential to perform comparative analysis of how control and mutant cell phenotypes develop over time in the same microenvironment. They also represent the only way to accurately study and model biological processes involving sporadic somatic mutations and their effect on cell proliferation, differentiation or competition.

In Drosophila, interchromosomal mitotic recombination associated with distinct tissue markers has been widely used to induce and track genetic mosaics. A similar approach, named as MADM (mosaic analysis with double markers), has been developed in mice allowing the labeling of control and mutant (gene knockout) cells with different fluorescent markers (Contreras et al., 2021; Zong, 2014; Zong et al., 2005). This method has the advantage of allowing the full correlation between the expression of a given fluorescent marker and the genetic status (wildtype, heterozygous or knockout) of the locus carrying the mutation, which significantly decreases the rate of false positives or false negatives. However, the method relies on difficult to achieve interchromosomal Cre-dependent recombination events, which overall leads to the generation of very few clones of labelled control and mutant cells in a tissue expressing the recombinase Cre. Due to the rare nature of the interchromosomal recombination events, these genetic mosaics cannot be efficiently induced with tamoxifen-inducible CreERT2 lines, which are weaker and only transiently active. In addition, this technology cannot be used in quiescent cells and requires the chromosomal genetic linkage between the engineered MADM elements and another gene mutation, which significantly complicates the required mouse breedings and genetics and limits its general applicability. MADM is also not compatible with epistasis analysis requiring the simultaneous loss-of-function of multiple genes present in distinct chromosomes, or with the immense variety of existing floxed genes (exons flanked by LoxP DNA sequences).

Given the higher complexity and limitations of MADM, the most widely used method to generate conditional somatic genetic-mosaics in the mouse still involves the much simpler CreERT2-dependent mosaic induction of floxed genes deletion. With this method, the location, timing and frequency of the

recombination events can be regulated by restricting the expression of CreERT2 to a given tissue, and by varying the timing and dosage of the CreERT2 ligand tamoxifen. This much simpler and alternative method needs the use of independent fluorescent reporters of Cre-recombination, in order to detect the cells having CreERT2 activity. However, several studies have shown that Cre-activity reporter alleles, only accurately report recombination of themselves, and cannot be used to reliably report recombination of other floxed alleles (Fernandez-Chacon et al., 2019; Liu et al., 2013; Schmidt-Supprian and Rajewsky, 2007). Though much easier to implement than MADM, CreERT2-dependent genetic mosaic approaches generate a high frequency of false positives and false negatives and should not be used to perform mosaic genetics.

To overcome the limitations of current methods for generating genetic mosaics in mice, we have developed *iFlpMosaics*. These consist of a large set of new genetic tools and mouse lines that enable FlpO-dependent-induction of multispectral and ratiometric mosaics of both wildtype and mutant cells in the same tissue of an animal. *iFlpMosaics* are compatible with the use of all existing floxed alleles and can be induced in any tissue quiescent or progenitor cells. They also allow a much tighter control over time of the frequency of genetic mosaicism. The multiple fluorescent labels match with high certainty the genetic status of the cells, that can be either control/wildtype or mutant for one or several genes. Since the multispectral and genetic barcoding of the cells is ratiometric, single-cell derived mutant and wildtype clonal expansion and differentiation can be profiled with high accuracy directly *in situ* through imaging or *ex situ* by FACS or scRNA-seq (single cell RNA-seq). *iFlpMosaics* will greatly facilitate the induction and analysis of somatic genetic mosaics and make possible the understanding how an individual or combinatorial set of genetic mutations affect the biology of single cells during tissue development, regeneration or disease.

False positives and false negatives with Cre-dependent mosaic genetics

Given its simplicity, CreERT2 genetics is still the most frequently used technique to induce genetic mosaics in mice. However, it is prone to induce a high frequency of false positives and false negatives. False positives are defined as cells recombining/expressing a reporter, and not having another independent floxed reporter or gene deleted. Conversely, false negatives are defined as cells not having a specific reporter allele recombined, but having another floxed reporter or gene deleted (Fig. 1a). The high frequency of false positive and false negative cells with CreERT2 genetics has been previously reported (Fernandez-Chacon *et al.*, 2019; Liu *et al.*, 2013) but so far no study has systematically quantified their occurrence for multiple reporter alleles and at lower induction rates or tamoxifen doses, that are needed for mosaic genetics. In order to do this, we decided to analyse several independent mice containing multiple Cre-reporters located in the Rosa26 locus, that could allow us to detect false

105 positives or negatives among different reporters by FACS or by histological analysis. This analysis
106 showed that different Cre-reporters, even when located in the same accessible Rosa26 locus, and having
107 similar genetic distances between LoxP sites, recombine at significant different relative frequencies
108 (Fig. 1b). As expected, the chance of finding cells having dual recombination of two reporters (true
109 positives) decreased with the decrease in the dose of induction or tamoxifen (Fig. 1c, 1d). It is important
110 to note that for single cell functional genetic/clonal analysis, usually it is necessary to decrease the dose
111 of tamoxifen in order to obtain sparse labelling of mutant or wildtype cells in the tissue. This means
112 achieving between 0.01-10% recombination rate, so that single cells and their clones can be
113 unequivocally distinguished. We found that even at around 10-60% average recombination rate for two
114 independent reporters, with similar sensitivities to CreERT2 and 4-Hydroxytamoxifen (4-OHT), the
115 rate of true positives was very low (Fig. 1c, 1d).
116 This data shows that Cre-reporters do not accurately report the recombination of any other
117 reporter, or floxed gene. Therefore, the large majority of CreERT2-based functional genetic studies *in*
118 *vivo* using mosaic genetics or sparse cell labelling, will not achieve the desired targeted gene deletion
119 in the labelled cells, and therefore will not be able to uncover the real effect of the gene on single cell
120 biology, with high accuracy and statistical power.
121
122 **Design and validation of *iFlp-Mosaic* mice**
123
124 To overcome the caveats of the CreERT2-dependent and MADM mosaic genetics
125 technologies mentioned above, we developed *iFlpMosaics*. This toolbox consists of several mouse lines
126 that allow the FlpO/FlpOERT2-recombinase-dependent induction of ratiometric mosaics of fluorescent
127 mutant (gene KO) and normal (gene wildtype) cells (Fig. 1e, 1f and Sup. Fig. 1a, b). We term these new
128 mouse alleles as *iFlp-Mosaics* (R26-$iFlp^{MTomato\text{-}Cre/MYFP}$ and Tg-$iFlp^{MTomato\text{-}H2B\text{-}GFP\text{-}Cre/MYFP\text{-}H2B\text{-}Cherry\text{-}FlpO}$).
129 They contain the ubiquitously expressed CAG promoter and several distinct and mutually exclusive
130 FRT sites (Cai et al., 2013), that enable multispectral labeling and fate-mapping of different mutant
131 cells expressing the fluorescent membrane-tagged tomato (MTomato) protein and Cre, and wildtype
132 cells expressing membrane tagged YFP (MYFP), in any tissue expressing FlpO or FlpOERT2. The two
133 lines differ either in the genomic location (ROSA26 versus random transgene), or the expression of
134 additional chromatin-bound (H2B-tag) fluorescent proteins for increased cellular resolution and
135 quantitative power (Fig. 1e, 1f and Sup. Fig. 1a, b).
136 Transfection of *iFlp-Mosaic* ES cells with FlpO expressing plasmids or induction of these
137 mosaics in mice carrying *FlpO/FlpOERT2* alleles, induced the expected ratiometric mosaic of cells
138 (Fig. 1e, 1f, and Supplementary Fig. 1c-g). The observed frequencies of recombination are in agreement
139 with the shorter genetic distance between the FRTF3 sites, in comparison with FRT5T2 sites (Fig. 1e
140 and Sup. Fig. 1a, b, e). In both ES cells and mice, the initially induced cellular ratios did not change

141 after prolonged culture or during tissue development *in vivo* (Fig. 1g and Sup. Fig. 1h), showing that
142 expression of MTomato-2A-Cre (or MYFP) is not deleterious to cells. Of note, we found on average
143 10 times less expression of the cassette MTomato-2A-Cre in *iFlp-Mosaic* mice than with the previously
144 generated *iSuRe-Cre* mice (Fig. 1h), which further reduces the occurrence of any potential Cre-toxicity
145 (Fernandez-Chacon *et al.*, 2019). This difference in expression is likely due to the different DNA
146 elements contained in these alleles or their different genomic location and epigenetic regulation.

147 Previously published inducible Cre-expressing alleles located in the Rosa26 locus have been
148 reported to be leaky and induce germline recombination, even in the absence of FlpO/CreERT2 activity
149 (Fernandez-Chacon *et al.*, 2019; Lao et al., 2012). Therefore, we checked if *iFlp-Mosaic* mice were
150 also leaky, given that the *iFlp-Mosaic* alleles contained a Cre and also FlpO expressing cassette, that
151 can be expressed if the upstream transcriptional stop signals are bypassed, as in previous mouse lines.
152 Importantly, none of the *iFlpMosaic* mice had leaky expression of the fluorescent proteins contained in
153 their constructs, in the absence of an extra allele expressing FlpO (Sup. Fig. 1i). The combination of
154 *iFlp-Mosaic* mice with the $Rosa26^{LSL\text{-}YFP}$ reporter mice, revealed a very low percentage of non-self Cre-
155 leakiness in some organs of the $Tg\text{-}iFlp^{Tomato\text{-}H2B\text{-}GFP\text{-}Cre/YFP\text{-}H2B\text{-}Cherry\text{-}FlpO}$ mouse line only. This
156 recombination occurs sporadically throughout embryonic development until adult stages, in the absence
157 of any FlpO activity, or any detectable *iFlp-Mosaic* fluorescent protein expression (Sup. Fig. 1i). This
158 residual Cre non-self-leakiness is likely due to residual and sporadic skipping or splicing of the 2 polyA
159 transcription STOP cassette that precede the ORF containing Cre, as shown before (Fernandez-Chacon
160 *et al.*, 2019; Lao *et al.*, 2012). Importantly, these very few false negative cells detected with the
161 $Rosa26^{LSL\text{-}YFP}$ Cre-reporter will never be detected or analysed with *iFlpMosaics*, since they are non-
162 fluorescent in the absence of other Cre-reporter alleles.

163 Significantly more relevant than false negatives, is the ocurrence of false positives. We found
164 that in i*FlpMosaic* mice, MTomato-2A-Cre+ cells efficiently recombine other Cre-reporter alleles and
165 all floxed genes tested (Fig. 1i. 1j), which ensures high genetic reliability at single cell resolution. As
166 an example, induction of *iFlpMosaics* in the *Rbpj* floxed background, results in only 3.5% Tomato-2A-
167 Cre+ cells in arteries and 96% in veins and capillaries (Fig. 1k), which is indicative of a high gene
168 deletion efficiency. Altogether, this data shows that with *iFlpMosaics* the rate of properly labelled and
169 assigned mutant and wildtype cells is very high. This is in stark contrast to standard CreERT2 mosaic
170 genetics (Fig. 1c, 1d), and similar to the MADM system (Contreras *et al.*, 2021; Zong, 2014; Zong *et*
171 *al.*, 2005). Therefore, *iFlpMosaic* alleles enable for the first time the tightly-controlled induction of
172 reliable and ratiometric mosaics of mutant and wildtype cells in any tissue expressing FlpO or
173 FlpOERT2, and provide both membrane and nuclei fluorescent markers to track mutant and wildtype
174 cells proliferation, differentiation or migration with very high cellular and quantitative resolution (Sup.
175 Fig. 2).
176

177 **Generation of ubiquitous and tissue-specific FlpOERT2 mouse lines**

178

179 Multispectral genetic mosaics are a particularly relevant research tool when is possible to
180 induce them at a specific time point and in a significant number of cells, which is not possible to achieve
181 with the MADM system (Contreras *et al.*, 2021; Zong, 2014; Zong *et al.*, 2005). To have temporal
182 control over Flp activity or induction, different mouse lines were generated in the past that enable the
183 constitutive (Rosa26) or tissue-specific expression of FlpeERT or the mammalian codon optimized
184 FlpOERT (Hunter et al., 2005; Kranz et al., 2010). These studies have shown that FlpOERT2 activity
185 is significantly lower than CreERT2, and very few cells in each organ were shown to recombine (Lao
186 *et al.*, 2012). In agreement with this, the published $R26^{CAG\text{-}FlpOERT2}$ line recombined the $R26\text{-}iFlp^{MTomato\text{-}Cre/MYFP}$
187 allele in only around 0.2% of most embryo cells, and was also weak in postnatal and adult organ
188 cells (Fig. 2a).

189 We therefore thought to develop new constructs containing optimized DNA elements (Cai *et*
190 *al.*, 2013; Pontes-Quero et al., 2017) in order to enhance FlpOERT2 expression (Fig. 2b). We generated
191 and screened in total 5 transgenic ubiquitous-FlpOERT2 mouse lines with variable copy number (Fig.
192 2c). Importantly, when comparing with the existing $R26^{CAG\text{-}FlpOERT2}$ line, the best of these new *Tg(Ins-*
193 *CAG-FlpOERT2)* lines (named here as, $Tg(Ins\text{-}CAG\text{-}FlpOERT2)^{\#F2}$) induced several fold higher
194 recombination of the *iFlpMosaic allele* in embryos and different organs and cell types (Fig. 2d-g and
195 Sup. Fig. 3a-d). With this higher frequency of recombination, we could frequently see mutant
196 (MTomato+) and wildtype (MYFP+) cells close to each other, which enables direct comparative
197 analysis of cells experiencing the same tissue microenvironment (Fig. 2f, 2g). Interestingly, the
198 recombination rate was not similar among different cell types and organs. We also confirmed that
199 despite the ubiquitous and strong expression of *FlpOERT2* by this new line, it is not leaky (Sup. Fig.
200 3e). Unlike the published $R26^{CAG\text{-}FlpOERT2}$ allele, this new transgenic allele can also be combined with
201 two other *Rosa26* targeted alleles, which is of high utility as it will be shown further below.

202 Besides generating ubiquitous *FlpOERT2* lines of general relevance, we also developed a
203 method to easily target and modify pre-existing and pre-validated *CreERT2* expressing transgenic
204 alleles, for tissue-specific expression of *FlpOERT2*. We designed unique guide RNAs and donor DNAs
205 containing FlpO that allow the efficient conversion of *CreERT2* alleles into a *FlpOERT2* expressing
206 allele (Fig. 2h). Using this method, we converted an existing PAC *Cdh5-CreERT2* mouse line (Wang
207 et al., 2010) containing 4 copies of the *CreERT2* sequence, to PAC *Cdh5-FlpOERT2* mouse lines
208 containing 3 or 4 copies of the *FlpOERT2* sequence (Fig. 2i). From the obtained two founder lines, only
209 the line $Cdh5\text{-}FlpOERT2^{F1}$ did not have any residual Cre sequence or activity (Fig. 2h). As expected,
210 this line was expressed and induced recombination specifically in endothelial cells (ECs, Fig.2j).

211

212 **Ratiometric functional genetics with *iFlp-Mosaic* mice**

213

214 In contrast to previous classical Cre-reporters or the *iSuRe-Cre* allele, *iFlpMosaics* are
215 ratiometric by design. This allows the quantification by histology or FACS of the relative frequencies
216 (ratio) of mutant (MTomato-2A-Cre+) and wildtype (MYFP+) cell populations induced exactly in the
217 same tissue, and experiencing the same microenvironment throughout the pulse-and-chase period. We
218 envisioned this property could be used to study in a high-throughput and accurate manner the cell-
219 autonomous function of genes in virtually all cell types, and for long time periods, something not
220 possible to be done with classical gene knockouts, because of their early lethality or major
221 abnormalities, or with classical Cre/CreERT2 mosaic genetics, because of the high frequency of false
222 positives/negatives (Fig. 1c, 1d), and the lack of an internal induction control of wildtype cells.

223 To demonstrate the power of *iFlpMosaic* mice to understand the effect of induced mutations in
224 multiple cell lineages we intercrossed them with either the *Tg(ACTFLPe)9205Dym* (Rodriguez et al.,
225 2000) allele (abbreviated as *ACTB:FlpE - recombines early embryo progenitor cells)*; the *Apln-FlpO*
226 (Luo et al., 2021) allele (recombines endothelial and derived hematopoietic cells) or the new *Tg(Ins-*
227 *CAG-FlpOERT2)* allele (induces recombination at any stage and in all cell type). These alleles were
228 further combined with floxed alleles for the genes *Myc and Foxos*. These genes are known to be
229 important for the proliferation and differentiation of many different cell types (Claveria et al., 2013;
230 Eijkelenboom and Burgering, 2013).

231 When the allele *R26-iFlp*$^{MTomato\text{-}Cre/MYFP}$ was combined with the *ACTB:FlpE* or *Apln-FlpO*
232 alleles and the *Myc and Foxos* floxed alleles, mosaic mutant animals survived until adult stages, unlike
233 embryos carrying mutations of these genes in all cells or in all ECs (Dharaneeswaran et al., 2014; He
234 et al., 2008). To understand how these genes affected the biology of different organ cell types, we first
235 used FACS analysis to score in a high throughput manner the relative ratios of mutant (MTomato-Cre+)
236 and wildtype cells (MYFP+) in several major organs of postnatal day 7 animals. The assumption was
237 that if a gene is really important for a given cell type/organ biology or lineage, it would either change
238 the proliferation or differentiation rate of the mutant cells, and that would be noticed in the final
239 MTomato+/MYFP+ log ratio detectable by FACS. This analysis revealed that the impact of MYC loss
240 varies in different cell types and organs. It was previously proposed that MYC loss leads to a general
241 competitive disadvantage (Claveria *et al.*, 2013) and lack of proliferation by ECs (Wilhelm et al., 2016),
242 however, when deleted mosaicly, it has a relatively minor effect on the clonal expansion of ECs (Fig.
243 3a). In contrast, we observed blood to be the most sensitive cell type to the mosaic loss of MYC (Fig.
244 3b and Sup. Fig. 4a, b). Most CD31-CD45- lung and heart cells were not significantly affected by *Myc*
245 deletion (Fig. 3c), likely due to compensation by the homologous *Mycn* gene (Munoz-Martin et al.,
246 2019).

247 We also confirmed the power of the system to perform mosaic epistasis analysis of mutant cells
248 with deletion of multiple genes, in this case 3 *Foxo* genes (6 floxed alleles). Foxos partially compensate
249 the function of each other in several cell types, and together they are considered to be important negative
250 regulators of cell proliferation and metabolism downstream of AKT signalling, preventing uncontrolled
251 cell growth (Eijkelenboom and Burgering, 2013; Paik et al., 2007; Wilhelm *et al.*, 2016). Surprisingly,
252 the results show that mosaic deletion of three *Foxo* genes (*Foxo1/3/4*^{KO}) had relatively minor
253 consequences for cell expansion in the liver and lung, and affected especially heart cells (Fig. 3d). This
254 suggests cell-type and organ-specific functions for *Foxos*. The data also showed that postnatal retina
255 ECs are especially responsive to the loss of *Foxo1/3/4*, as they were much more proliferative, formed
256 dense EC clusters, and outcompeted wildtype cells over time (Fig. 3e), in line with the vascular
257 phenotypes and hemangiomas shown before using standard CreERT2 genetics (Paik *et al.*, 2007;
258 Wilhelm *et al.*, 2016).

259 Overall, these results show the power of this technology to accurately model and analyse in a
260 high-throughput manner by FACS, or tissue imaging, the impact of somatic mutations in cellular
261 expansion and competition. In this particular case, it revealed that MYC and FOXOS are dispensable
262 for the proliferation of many types of cells in diverse organs, being MYC mostly relevant in the blood
263 lineage and FOXOS in ECs.

264

265 **Combining *iFlp-Mosaic* with *iFlp*^{Chromatin} for higher single-cell clonal resolution**

266

267 Direct live imaging of Cre-mutant and adjacent normal fluorescent cells can be one of the main
268 applications of the *iFlp-Mosaic* technology. However, even though live microscopic imaging is routine in
269 many species and developmental model systems, it is still not possible, or practical, for most mouse tissues and
270 laboratories, due to the deep tissue location of most cells in the mouse, lack of appropriate microscopes, or the
271 relatively slow pace of the biological processes under study. To analyse how single cells proliferate,
272 differentiate and migrate in a mouse tissue advanced pulse-and-chase genetic and imaging/analysis tools are
273 required. Genetic tools such as the *Brainbow*, *Confetti* or the *Dual ifgMosaic* were generated for this purpose
274 (Livet et al., 2007; Pontes-Quero *et al.*, 2017; Snippert et al., 2010). When compared with standard unicolor or
275 single-molecule reporters of Cre activity, multispectral mosaics allow a more precise and quantitative single-
276 cell retrospective and clonal lineage tracing, due to the lower probability of a cell having a given stochastic
277 recombination event or barcode. To increase the quantitative single cell resolution of the *iFlp-Mosaic*
278 technology, we combined the *Rosa26-iFlp*$^{MTomato\text{-}Cre/MYFP}$ allele with the published *Rosa26-iChr2-Mosaic* (or
279 iCre$^{H2B\text{-}Cherry/GFP/Cerulean}$, see Sup. Fig. 4c) allele (Pontes-Quero *et al.*, 2017). These enables the stochastic and
280 mutually exclusive expression of both chromatin/nuclei (for cell unit count) and membrane (for cell shape)

281 localized fluorescent proteins in mutant (MTomato-2A-Cre+) cells, expanding the diversity of cell barcoding
282 from 1 to 3 different possible mutant cells (Fig. 4a).

283 Despite higher clonal resolution in single MTomato+/mutant cells, this method does not allow us to
284 quantify in the same microenvironment, and with the same level of resolution, how the MYFP+/wildtype cells
285 clonally expand. In order to have higher clonal resolution also in wildtype cells, we developed the *iFlp*^{Chromatin}
286 (or *iFlp*$^{H2B\text{-}Cherry/GFP/Cerulean}$) mouse line, in which three distinct and incompatible FRT sites enable the generation
287 of a Flp-recombinase-dependent mosaic of cells expressing three distinct chromatin (H2B-tag) localized
288 fluorescent proteins (Fig. 4b, 4c). When interbred with the *Tg(Ins-CAG-FlpOERT2)* and *iFlp*$^{MTomato\text{-}Cre/MYFP}$-
289 *Mosaic* lines, this new *iFlp*^{Chromatin} allele allow us to generate up to 8 different dual-labelled cells (4 mutant
290 and 4 wildtype), significantly increasing the single-cell clonal lineage tracing resolution of both mutant and
291 wildtype cells in the same tissue microenvironment (Fig. 4d). The alleles above can also be combined with
292 the published Cre-dependent Tg(*iMb2-Mosaic*) allele (or *iCre*$^{MYFP/Tomato/MTFP1}$) (Pontes-Quero *et al.*, 2017),
293 to have even higher single-cell or clonal resolution on mutant (Tomato+ with 12 different fluorescent barcodes)
294 and wildtype (YFP+ with 4 different fluorescent barcodes, or YFP- with 3 different barcodes) cells (Fig. 4e).
295 This technology also allows us to label and identify binucleated and polyploid cells, such as adult liver
296 hepatocytes (Fig. 4f).

297

298 **Single cell functional mosaic genetics with iFlp-Mosaics**

299

300 As an example, we show here how these new mouse alleles and technology enabled us to
301 achieve very high cellular resolution, and to accurately quantify how single mutant and wildtype cells
302 clonally expand, migrate, or survive, when induced at the same time, in the same tissue microenvironment.

303 In the liver, a high percentage of neonatal hepatocytes are in s-phase (EdU+) or in cycle (Ki67+)
304 at P1 and P7 and most stop dividing before P20 (Fig. 5a), however their single cell clonal expansion
305 dynamics is still unknown. *iFlp-Mosaic x iFlp*^{Chromatin} mice were induced at P1 and livers collected at P20 for
306 multispectral imaging and single-cell clonal analysis. Multispectral confocal scanning and spatial mapping of
307 clones revealed that hepatocyte proliferation (clones with 2 cells or more) were dispersed across the liver (Fig.
308 5b and Sup. Fig. 5a,b). The recombination frequency varied among animals, but the average clone size was
309 still similar (Fig. 5c), confirming that there is enough multispectral clonal and quantitative resolution at both
310 low and high *iFlp-Mosaic* recombination frequencies. This data revealed that 17,2% of neonatal hepatocytes
311 did not expand clonally, with the majority of hepatocytes (69%) dividing only once or twice in 20 days. Only
312 2.4% of single hepatocytes gave clones with 8 or more cells. The average clone size of wildtype cells was
313 around 2.9, in agreement with the observed 2.9-fold liver weight increase from P1 to 20 (Fig. 5c, d). We then
314 compared the clonal expansion of wildtype (MYFP+) and mutant *Myc*^{KO} (Mtomato-2A-Cre+) hepatocytes.

315 This revealed that MYC is necessary for optimal postnatal hepatocytes clonal expansion. On average, *Myc*^{KO}
316 hepatocytes clone size was 2.25 and these generated only 125% (125 new hepatocytes for each 100) more
317 hepatocytes over 20 days, whereas wildtype cells clone size was 2.87 and these generated 187% more
318 hepatocytes, over the same period (Fig. 5e, f).

319 We next performed a similar single cell clonal expansion analysis of postnatal pancreatic cells. These
320 cells had similar Ki67+ and EdU+ frequencies as liver cells (compare Fig.5a with Sup. Fig. 5c, d). However,
321 *iFlpMosaics* analysis revealed that wildtype pancreatic cells expand significantly more than hepatocytes until
322 P20 (Fig. 5g), with an average clone size of 3.60 instead of 2.87 (compare Wt values in Fig. 5h,i with Fig.5e,f).
323 In the pancreas, *Myc*^{KO} cells also expanded significantly less (Fig. 5h, 5i) and at the end were 3.7 fold less
324 frequent than neighbouring wildtype cells (Fig. 5j).

325 Recent work proposed the existence of a highly proliferative hepatocyte population in adult livers,
326 based on a new Dre-inducible Ki67-Cre (ProTracer) allele (He et al., 2021) or CreERT2-based single cell
327 lineage tracing of a unicolor reporter (Wei et al., 2021). Ki67 immunostaining showed that only 1.87% of adult
328 liver hepatocytes are in cycle at a given moment (Sup. Fig.5d). Of note, Ki67 may be expressed in metabolically
329 activated (primed and in cycle) or DNA replicating (S-phase), or polyploid cells, but many Ki67+ cells may
330 not undergo productive cell division, or die after being in cycle. Our *iFlpMosaics* can measure both productive
331 cell expansion or cell survival. Using the *iFlpMosaic* mice with the highest number of multispectral
332 combinations, and therefore single cell clonal resolution, we observed very limited proliferation or clonal
333 expansion of single mononucleated or binucleated hepatocytes during the 2 weeks after induction. Average
334 clone size of adult hepatocytes was only 1.10 after 2 weeks (Fig. 5k, l), significantly lower than the 1.38 after
335 only 1 week of pulsing shown before using a simpler unicolor reporter (Wei *et al.*, 2021). In 2 weeks, only
336 9.5% of single mononucleated or binucleated diploid hepatocytes underwent productive division or cytokinesis
337 from binucleated cells to form a 2-cell clone (Fig. 5m, n). Frequency of proliferation was also low among
338 polyploid hepatocytes (4.9%). This data significantly extends on the recent analysis of hepatocytes
339 proliferation dynamics using different technologies (He *et al.*, 2021; Wei *et al.*, 2021).

340 Despite the absence of significant hepatocytes proliferation in homeostasis, when we induced the *iFlp*
341 ratiometric mosaics in adult *Myc*^{flox} livers, we still observed a very significant loss (4.2 fold decrease) of mutant
342 *Myc*^{KO} cells in only 2 weeks after induction (Fig. 5o). Given the absence of significant clonal expansion of
343 wildtype cells in adult livers (Fig. 5l - average clone size 1.10, meaning only 10 more hepatocytes for each 100
344 hepatocytes in 2 weeks), this data suggests that Myc loss induces a significant decrease in adult hepatocytes
345 survival. Interestingly, wildtype hepatocytes when surrounded by *Myc*^{KO} hepatocytes expanded more than
346 when surrounded by wildtype hepatocytes (compare Fig. 5m/n with 5p/q and Sup. Fig.5e), probably to
347 compensate for the loss of *Myc*^{KO} hepatocytes. This data suggests the existence of a Myc-dependent cell
348 competition among adult hepatocytes, in which cells with lower Myc are less fit and gradually excluded, as
349 shown before to occur during early embryonic development (Claveria *et al.*, 2013). This competition and cell

350 turnover may explain why liver cell mass does not increase over time, despite having constant cell proliferation.
351 Among the surviving *Myc*^{KO} mutant cells, we also observed a significant increase in the % of binucleated cells,
352 and a decrease in the % of 2-cell mononucleated clones, suggesting that *Myc*^{KO} binucleated hepatocytes
353 undergo cytokinesis less frequently (Sup. Fig. 5e).

354

355 **$iFlp/Dre^{Progenitor}$ enables induction of genetic mosaics from single progenitor cells**

356

357 The results above show also that there is significant intercellular clonal variability, when
358 different progenitor cells, occupying different tissue locations, are induced. This decreases the statistical
359 robustness of the analysis of a gene function in single cells and requires the comparative analysis of a
360 large number of single-cell derived clones, and averaging of clone size differences. With the method
361 above, averaging and population comparisons can be made among all Tomato+ and all YFP+ clones
362 found in a region. However, since they derive from different progenitor cells, is not possible to know
363 exactly how a gene loss, changes the cellular and clonal expansion phenotype of a specific single-cell
364 progeny, located in a particular niche. The existent MADM approach allows the generation of labelled
365 wildtype and mutant cells from the same progenitor cell, and in this way estimate very precisely how a
366 gene mutation impacts on the progeny single cell mobilization and proliferation phenotypes. However,
367 as mentioned above, MADM is very difficult to implement and induce at a specific time point, nor it is
368 compatible with the numerous existent floxed genes.
369 To overcome the limitations of current approaches to understand the role of genes in single
370 progenitor cell biology, we designed the $iFlp/Dre^{Progenitor}$ DNA construct (Fig. 6a). This was injected in
371 mouse eggs to produce transgenic animals, of which only one of four founders was good and named as
372 $iFlp/Dre^{ProgenitorF1}$. We also knocked-in this construct by CRISPR-Cas9 in the *Tg(Ins-CAG-*
373 *FlpOERT2)*$^{\#F4}$ locus creating the dual *Tg(Ins-CAG-FlpOERT2 + iFlp/Dre*^{ProgenitorF2}*)* allele (Fig. 6b).
374 These $iFlp/Dre^{Progenitor}$ alleles can be induced by both FlpOERT2, or the stronger DreERT2. Therefore,
375 we also generated a new *Tg(Ins-CAG-DreERT2)*$^{\#F4}$ allele by using CRISPR/Cas9 assisted targeting into
376 the pre-existent and screened *Tg(Ins-CAG-FlpOERT2)* allele (Fig. 6c). We hypothesized that when
377 these alleles are combined with *iFlpMosaic* alleles, it will be possible to induce with tamoxifen a genetic
378 cascade that culminates with the generation of genetic mosaics of mutant and wildtype cells derived
379 from the same single progenitor cell. After tamoxifen induction of FlpOERT2 or DreERT2, the
380 $iFlp/Dre^{Progenitor}$ allele is recombined, and this triggers the constitutive expression of FlpO, H2B-V5 and
381 the cell-surface marker hCD2. FlpO will than effectively recombine in H2B-V5+/hCD2+ cells the *R26-*
382 *iFlp*$^{MTomato\text{-}Cre/MYFP}$ allele (Fig. 6d). We hypothesized that since FlpO is a relatively weak recombinase
383 and the transgene takes some time to be fully expressed, it could also take time to recombine the *R26-*
384 *iFlp*$^{MTomato\text{-}Cre/MYFP}$ allele. During this period, a dividing cell will often generate two or more daughter

385 cells, and in these, the *iFlpMosaic* allele can be recombined in one of two possible ways, generating
386 either Tomato-2A-Cre+ or YFP+ cells within the progeny of a single cell.
387 To test this hypothesis, we induced growing animals with low dose of tamoxifen at P4, and
388 collected tissues for analysis 3 days later at P7. In animals without the *iFlp/Dre*^{Progenitor} allele, Tomato+
389 and YFP+ cells arised from independent progenitors that were genetically pulsed in independent
390 locations and rarely YFP+ wildtype cells were intermixed with mutant Tomato+ cells (Fig. 6e). In
391 animals having the *iFlp/Dre*^{Progenitor} allele, anti-V5 immunostaining enabled the detection of the nuclei
392 of the progenitor cell and its progeny. V5+Tomato+ and V5+YFP+ cells were frequently located close
393 to each other confirming that they arised from a single progenitor cell (Fig. 6f and Sup. Fig. 6a), which
394 allows for direct comparisons of a gene function in the progeny of single progenitor cells.
395 Importantly, the use of the *iFlp/Dre*^{Progenitor} allele also allowed us to significantly increase the
396 sensitivity (14 fold) to FlpOERT2 recombination. With the Cdh5-FlpOERT2 line, we increased EC-
397 recombination efficiency from an average of 3.6% to 51% (Fig. 6g). The use of the *iFlp/Dre*^{Progenitor}
398 allele together with *Tg(Ins-CAG-DreERT2)*$^{\#F4}$, instead of *Tg(Ins-CAG-FlpOERT2)*$^{\#F4}$, allowed a
399 significant increase in the efficiency of recombination as well (Fig. 6h).
400 Another advantage of the *iFlp/Dre*^{Progenitor} allele is the possibility of using anti-hCD2 magnetic
401 beads or antibodies to quickly isolate the recombined cells, even when their frequency is very low.
402 hCD2+ cells had a 25-fold higher % of Tomato+ and YFP+ cells (Fig. 6i), resulting in a much faster
403 isolation of these cells, which is important when when many tissues or infrequent populations have to
404 be isolated on the same day for scRNA-seq analysis.
405
406 **scRNA-seq of ratiometric *iFlp*^{Mosaics} to uncover gene function in all cell types**
407
408 Recent advances in scRNA-seq methods have allowed the understanding of single-cell biology in an
409 unprecedented way. There are however three main limitations on the use of scRNA-seq technologies to assess
410 the transcriptome of single mutant and wildtype cells resulting from conditional genetic experiments. The first
411 is the introduction of microenvironment changes bias by the profiling of cells obtained from distinct mutant
412 and wildtype animals, that experienced distinct epigenetic and microenvironmental changes during their
413 lifetime or in disease. The second, the reliance on standard Cre-reporters to define and isolate the mutant cells
414 of interest, since, as we showed above (Fig. 1), they do not correlate with desired genetic deletions, particularly
415 in CreERT2 inducible experiments. And the third, and most important, the difficulty in knowing a priori that
416 the desired floxed gene will be deleted among the pool of analysed and sequenced mutant single cells. This is
417 important because scRNA-seq technologies only detect the mRNA of some genes in most single cells, and
418 also because many floxed genes conserve their 3´ mRNA sequences after genetic deletion, leading to
419 the transcriptional profile of pseudomutant cells whose true genetic status cannot be accurately
420 determined.

We have provided evidence that in contrast to other genetic technologies, the *iFlp-Mosaic* alleles here developed allow the reliable isolation of *bona fide* mutant cells and wildtype cells from the same tissue (Fig. 1 and 2). We also provided evidence how ratiometric *iFlp-Mosaic* cell population genetics based on FACS or histology can be used to easily score the role of genes in single cell biology. Therefore, we decided to test if we could also use scRNA-seq with *iFlpMosaics* to score in a high throughput manner the role of genes (i.e. *Rbpj*) in the proliferation and differentiation of all early embryo cell types. *Rbpj* codes for a transcription factor essential for all Notch signalling, and this is one of the most important pathways for cell proliferation and differentiation during embryonic development (Siebel and Lendahl, 2017). We pulsed embryos with 4-OHT at embryonic day 9.5 (E9.5) and collected Tomato+ (mutant) and YFP+ (wildtype) cells by FACS at E13.5 (Fig. 7a). 16 major cell types were identified based on their transcriptome and previously known marker genes (Fig. 7b). In Tomato-2A-Cre+ cells, *Rbpj* deletion of the exons 6 and 7 generates a more unstable, but still detectable 3´mRNA (Fernandez-Chacon et al., 2023), and a decrease in the expression of *Rbpj* and the main downstream target *Hes1* (Fig. 7c). The canonical *Hes* and *Hey* genes can also be regulated by other pathways. Deletion of *Rbpj* led to changes in the frequency of cells in S-phase (Ki67+ mRNA) in some clusters (Fig. 7c). Global *iFlp-Mosaic* driven *Rbpj* deletion at E9.5, compromised the differentiation or expansion of peripheric nervous system, ECs, cardiomyocytes, erythrocytes, hepatocytes and myocytes cells, whereas epithelial and mesenchymal cells became more frequent (Fig. 7d-e). *Rbpj* deletion led to a 5 fold decrease in the frequency of ECs (Fig.7d, e**)**, loss of expression of the arterial marker genes *Gja5* and *Gja4*, and upregulation of the tip cell genes *Esm1, Kcne3, Apln* and *Cdkn1a* (Fig.7g,h). This correlates with its essential role in the specification of arterial ECs and inhibition of tip ECs (Luo *et al.*, 2021; Pontes-Quero et al., 2019). $Rbpj^{KO}$ ECs also upregulated genes related with epithelia-to-mesenchymal transition, glycolysis and angiogenesis and were less in cycle (Fig.7i). Analysis of other cell types scRNAseq data revealed that *Rbpj* loss changes the relative frequency of specific cell types clusters, suggesting an impact of this gene in their proliferation or differentiation. Indeed, different genes and genetic pathways were deregulated after *Rbpj* deletion in the many cell types and clusters identified (Fig. 7j-r and Sup. Fig. 7). This scRNA-seq data provides an important resource to further explore the role of Rbpj/Notch in the early expansion and differentiation of embryonic lineages. It also provides an example how the combination of ratiometric *iFlpMosaics* with scRNA-seq analysis can be very powerful to determine, in a high-throughput manner, a gene cell-autonomous function in all cell types during development or in disease.

456 **Discussion**

457

458 Genetic mosaics are essential to determine a gene cell-autonomous function, and prevent confounding
459 effects frequently associated to classical whole animal or tissue-specific conditional genetics. With
460 inducible mosaic genetics, the mutant and wildtype cells share the same microenvironment and
461 developmental or physiological history, being the only difference between them the deleted gene. This
462 provides a much more accurate way to study and understand a gene cell-autonomous function during
463 tissue development, homeostasis or in disease.

464 We and others have observed that the transcriptional programs and phenotype of single mutant cells in
465 genetic mosaics, are often very different from the programs and phenotypes of single cells extracted
466 from a tissue in which that gene was deleted in most of the tissue cells (Hansen *et al.*, 2022). Performing
467 comparative omics of mutant and wildtype cells in genetic mosaics will more accurately reveal the true
468 gene molecular and cellular function. With classical genetics, the changes in the mutant tissue function
469 and its microenvironment can always impact the transcriptional program of the mutant cells in ways
470 that are unrelated with the original gene function or genetic program. As an example, if a gene impairs
471 vascular development or permeability, the entire surrounding tissue growth, function and paracrine
472 signals will be affected, and these in turn will influence the mutant cells phenotype. With genetic
473 mosaics, these effects are controlled for, because the wildtype and mutant cells used for comparison
474 and omics analysis share the same history and microenvironment.

475 The most frequently used methods to perform mosaic conditional genetics in mice, the most widely
476 used model in biomedical research, have several caveats. Genetic mosaics induced by CreERT2 are
477 easy to achieve, but are unreliable (Fernandez-Chacon *et al.*, 2019; Liu *et al.*, 2013; Schmidt-Supprian
478 and Rajewsky, 2007). These also lack the co-induction of wildtype cells labelling for direct phenotypic
479 comparisons with the mutant cells. MADM is genetically very reliable, and provides an internal control,
480 but is a cumbersome and inefficient method, providing no temporal resolution in the induction and
481 genetic analysis (Contreras *et al.*, 2021; Zong, 2014; Zong *et al.*, 2005).

482 The set of new genetic tools described here significantly improve on these two technologies. In contrast
483 to Cre-ERT2 genetics, *iFlpMosaics* provide clearly distinguishable and reliable fluorescent labels for
484 both mutant (Tomato) and wildtype (YFP) cells. The simultaneous and ratiometric induction of both
485 mutant and wildtype cells fluorescent labels, in the same tissue, is very important, since it provides a
486 way to accurately measure and compare how these cells differ in their proliferation, differentiation,
487 migration or survival over time. We have shown that this ratiometric analysis can be done over short or
488 long periods of time. The fluorescent markers are easily detectable and quantifiable by both microscopic
489 imaging or FACS. In contrast to MADM, *iFlpMosaics* provide a high degree of inducibility, at any
490 specific time point and in any cell type, including quiescent cells present in adult mice, which will be

491 very important to model the etiology of diseases caused by sporadic somatic mutations, or to model the
492 consequences of CRISPR-based gene targeting/editing, that are by nature also mosaic. In addition,
493 *iFlpMosaics* are compatible with all existent mouse floxed alleles, being possible to mosaicly delete
494 one or multiple floxed genes in cis, which will be essential for genetic functional epistasis analysis, with
495 single-cell resolution. With *iFlpMosaics,* instead of only 1 cell barcode (as in standard CreERT2 or
496 MADM), up to 12 different multispectral barcodes for mutant cells and up to 7 for wildtype cells are
497 possible. This significantly higher spectral barcode diversity, and dual labelling (membrane and nuclei)
498 also significantly increase single cell and clonal quantitative resolution during a pulse-and-chase genetic
499 experiment.

500 In *iFlpMosaics,* cells expressing MTomato also express Cre, a recombinase shown before to be toxic
501 when expressed at high levels (Loonstra et al., 2001; Naiche and Papaioannou, 2007; Rashbrook et al.,
502 2022). However, we found that the expression of the *iFlpMosaic* alleles is relatively low, when
503 compared with previously published Cre-expressing lines (Fernandez-Chacon *et al.*, 2019). This can be
504 due to the different DNA elements used, and the presence of only one upstream insulator during Rosa26
505 targeting. It has been shown that the PGK-Neo cassette and the 2A peptide elements used in i*FlpMosaic*
506 alleles reduce the expression or translation efficiency (Ema et al., 2006; Pontes-Quero *et al.*, 2017;
507 Sharma et al., 2012). The absence of Cre toxicity with *iFlpMosaics* was confirmed by the analysis of
508 the relative ratio of Tomato-2A-Cre+/YFP+ cells over long periods of time *in vitro* and *in vivo*. This
509 ratio was kept constant over time when in a wildtype genetic background.

510 Single cell biology during tissue development is highly heterogenous, and therefore is also
511 important to be able to reliably induce and analyse genetic mosaics of mutant and wildtype cells derived
512 from single progenitor cells and with a minimal amount of false positives and false negatives. The
513 previously established MADM technology is ideal for this (Contreras *et al.*, 2021; Zong, 2014; Zong *et*
514 *al.*, 2005), but it lacks temporal inducibility and efficiency. With the new *iFlp/Dre*^{Progenitor} allele, we
515 were able to significantly increase the inducibility and precision of *iFlpMosaics*. The *iFlp/Dre*^{Progenitor}
516 allele FRT/Rox cassette, or genomic locus, is very sensitive to FlpOERT2/DreERT2 activity, and results
517 in a genetic cascade with a delay in the expression of FlpO, that is very convenient to generate different
518 mutant and wildtype cells within the progeny of a single progenitor cell, something only possible to
519 achieve so far with MADM. The progeny cells will also permanently express the nuclei marker H2B-
520 V5 and the surface marker hCD2, ideal for FACS or quick magnetic isolation of the cells.

521 Integration of information arising from *in situ* single-cell lineage-tracing microscopy methods, with
522 information derived from new scOMICs and bioinformatic analysis methods, will be essential to establish the
523 biology of single-cell lineages with high detail and in a realiable and high-throughput manner. We showed
524 how the combination of *iFlpMosaics* with FACS or scRNA-seq analysis provide an easy way to analyse
525 in a high-througput manner the cell-autonomous function of any gene in all cell types, during
526 development, homeostasis or disease. Since the mosaics of mutant and wildtype cells can be induced in

527 less than 10% of the animal cells, they will not severely affect tissue or organ development/homeostasis,
528 allowing analysis of the transcriptional, epigenetic, proliferative or differentiation state of all mutant
529 cells in a mostly wildtype environment. This means that crossing a floxed gene with multiple
530 independent CreERT2 lines (one for each cell type), is no longer needed to understand its cell-
531 autonomous function. The ubiquituous and strongly expressed FlpOERT2 and DreERT2 lines generated
532 here allow induction of *iFlpMosaics* in all cell types, at both low or high frequencies. This enables
533 direct comparisons of the molecular and cellular phenotypes of mutant and wildtype cells extracted
534 from all tissues of an embryo or animal.
535 *iFlpMosaics* will greatly facilitate the induction and high-throughput functional analysis of
536 somatic mutations or genetic mosaics. This will be key to understand how an individual or
537 combinatorial set of genetic mutations affect the biology of single cells during tissue development,
538 regeneration or disease.
539
540

541 # Methods

542

543 ## Mice

544

545 We generated and used Mus musculus with C57BL6 or C57BL6×129SV or B6CBAF1 genetic
546 backgrounds. All mice were backcrossed to C57Bl6 for at least a few generations. To generate mice for
547 analysis, we intercrossed mice with an age range between 7 and 30 weeks. We do not expect our data
548 to be influenced by mouse sex. The following mouse lines and alleles were used and interbred:
549 *Tg(Cdh5-CreERT2)* (Wang *et al.*, 2010), *Tg(iSuRe-Cre)* (Fernandez-Chacon *et al.*, 2019), *Notch1*$^{flox/flox}$
550 (Radtke et al., 1999), *Rbpj*$^{flox/flox}$ (Han et al., 2002), *Myc*$^{flox/flox}$ (de Alboran et al., 2001),
551 *Mycn*$^{flox/flox}$(Knoepfler et al., 2002), *Foxo1/3/4*$^{flox/flox}$(Paik *et al.*, 2007), *Rosa26-EYFP (Srinivas et al.,*
552 *2001), Rosa26-iChr2-Mosaic* (Pontes-Quero *et al.*, 2017), Tg-*iMb2-Mosaic or iCre*$^{MYFP/Tomato/MTFP1}$
553 (Pontes-Quero *et al.*, 2017), *Gt(Rosa)26*$^{tm3(CAG-FlpOERT2)Ali}$(Lao *et al.*, 2012), *Gt(Rosa)26Sor*$^{tm14(CAG-LSL-}$
554 $^{tdTomato)Hze}$(Madisen et al., 2010) and *Apln-FlpO* (Luo et al., 2021). The following mouse lines were
555 produced in this study: *R26-iFlp*$^{MTomato-Cre/MYFP}$, *Tg-iFlp*$^{MTomato-H2B-GFP-Cre/MYFP-H2B-Cherry-FlpO}$, *Tg(INS-CAG-*
556 *FlpOERT2), Tg(INS-CAG-DreERT2), Tg(Cdh5-FlpOERT2), iFlp*^{Chromatin}*-Mosaic* and *Tg-iFlp/Dre*^{Progenitor}.

557 *Tg-iFlp*$^{MTomato-H2B-GFP-Cre/MYFP-H2B-Cherry-FlpO}$, *Tg(INS-CAG-FlpOERT2), TgiFlp*^{Chromatin}*-Mosaic* and
558 *Tg-iFlp/Dre-Progenitor* mouse alleles were generated by standard DNA injection in mouse eggs and screening
559 of several transgenic founders as indicated in the main text or figures. The *R26-iFlp*$^{MTomato-Cre/MYFP}$ allele was
560 generated by CRISPR-assisted gene targeting in G4 ES cells of the Rosa26 locus using the guide
561 GACTGGAGTTGCAGATCACGA_GGG (IdT DNA) and a Donor DNA with the elements indicated

562 in Figure 1. Targeted ES cells were used for mice production. The *Tg(Cdh5-FlpOERT2)* line was
563 generated by CRISPR-Cas9-assisted gene targeting using mouse eggs of the existing *Tg(Cdh5-*
564 *CreERT2)* line (Wang et al., 2010) with the guide AAGCTTATCGATACCGTCGA_CGG and a donor
565 DNA containing either the Cdh5-FlpOERT2 sequence. *Tg(INS-CAG-DreERT2)* mice were generated
566 by CRISPR-Cas9 using guide RNAs (GATGTCGAACTGGCTCATGG_TGG and
567 AACAGGCGGATCTGCGTACG_CGG) targeting the existing FlpO sequence contained in the pre-
568 screened *Tg(INS-CAG-FlpOERT2)* transgene, and a donor DNA containing the *CAG-DreERT2*
569 sequence. Injections mixtures were composed by the described crRNAs (IDT) and tracrRNA (IDT,
570 catalog 1072533) at 0.305 microM and Cas9 nuclease (Alt-R® S.p. HiFi Cas9 Nuclease V3, 100 µg,
571 Catalog 1081060) at 20 ng/microL. Founders were initially screened by PCR with the primers described
572 in Supplementary Table 1.

573 To induce CreERT2, FlpOERT2 or DreERT2 activity in adult mice, 1g tamoxifen (Sigma-
574 Aldrich, P5648_1G) were dissolved in 50ml corn oil (20 mg/ml tamoxifen) and aliquots stored at -20C.
575 From this stock solution, animals were given intraperitoneal injection of 50µl to 100µl (total dose of 1
576 to 3 mg tamoxifen per animal at 40 to 120 mg/kg) as indicated in figures. In pregnant females, the
577 tamoxifen was dissolved together with progesterone to reduce miscarriage (2mg tamoxifen and 1mg
578 progesterone per female). To activate recombination in pups, 4-OHT was injected at the indicated stages
579 at a dose of 40 mg/kg body weight or 4mg/kg, in the case of low dose, as indicated in the figures. All
580 mouse lines and primer sequences required to genotype these mice are provided in Supplementary Table
581 1.

582 All mouse husbandry and experimentation were conducted using protocols approved by local
583 animal ethics committees and authorities (Comunidad Autónoma de Madrid and Universidad
584 Autónoma de Madrid CAM-PROEX 177/14, CAM-PROEX 167/17, CAM-PROEX 164.8/20 and
585 PROEX 293.1/22). The mouse colonies (Mus musculus) were maintained in racks with individual
586 ventilation cages according to current national legislation. Mice have dust/pathogen-free bedding, and
587 sufficient nesting and environmental enrichment material for the development of species-specific
588 behavior. All mice have 'ad libitum' access to food and water in environmental conditions of 45–65%
589 relative humidity, temperatures of 21–24 °C, and a 12 h/12 h light/dark cycle. In addition, and to
590 preserve animal welfare, mouse health is monitored with an animal health surveillance program, which
591 follows FELASA recommendations for specific pathogen-free facilities.

592

593 **Immunofluorescence on cryosections**

594

595 For multispectral *iFlp-Mosaic* tissue harvesting, mice were euthanized in CO2 chambers, then
596 10 ml of KCl 50 mM were injected in the left ventricles and whole mice were perfused with pH 7

formaldehyde 3.7-4 % (ITW Reagents, 252931). Explanted tissues were post-fixed for 2 h in 4% PFA (Thermoscientific, 043368.9M) in PBS at 4°C and under gentle rotation. After three washes in PBS for 10 min each, organs were stored overnight in 30% sucrose (Sigma) in PBS. Organs were then embedded in OCT™ (Sakura) and frozen at -80°C. Cryosections (35 µm) were cut on a cryostat (Leica), washed three times for 10 min each in PBS, and blocked and permeabilized in PBS containing 10% donkey serum (Milipore), 10% fetal bovine serum (FBS), and 1% Triton X-100. Primary antibodies were diluted in blocking/permeabilization buffer and incubated overnight at 4°C. This step was followed by three 10 min washes in PBS and incubation for 2 h with conjugated secondary antibodies (1:200, Jackson Laboratories) and DAPI in PBS at room temperature. After three washes in PBS, sections were mounted with Fluoromount-G (SouthernBiotech). All antibodies used are listed in Supplementary Table 2.

Wholemount Immunofluorescence of retinas

For postnatal mouse retina immunostaining, eyes were collected and fixed in ice cold 4% PFA in PBS for 10 minutes. After fixed for 15 minutes more at room temperature. After washed once in PBS and kept on ice. After microdissection with spring scissors (FST), retinas were fixed in 4% PFA for an additional 45 min at room temperature, followed by two PBS washes of 10 min each. Retinas were blocked and permeabilized with PBTS buffer (0.3% Triton X-100, 3% fetal bovine serum (FBS) and 3% donkey serum) for 1 h. Samples were then incubated overnight at 4 °C in Biotinylated isolectinB4 (Vector Labs, B-1205, diluted 1:50) and primary antibodies (Supplementary Table 2) diluted in PBTS buffer. After five washes (20 min each) in PBTS buffer diluted 1:2, samples were incubated for 2 h at room temperature with Alexa conjugated secondary antibodies (Supplementary Table 2). After three washes of 30 min each in PBTS buffer (diluted 1:2), and two washes of 15 min each in PBS, retinas were mounted with Fluoromount-G (SouthernBiotech).

In vivo EdU labelling and EC proliferation detection

To detect EC proliferation in postnatal livers and pancreas, 20 µg g^{-1} body weight EdU (Invitrogen, A10044) was injected intraperitoneally into P1, P7 or P20 mice 4h before dissection. Livers and pancreas were fixed in PFA4% and processed for OCT cryoblocks and sections as mentioned above. EdU signals were detected with the Click-it EdU Alexa Fluor 647 or 488 Imaging Kit (Invitrogen, C10340 or C10337). In brief, after all other primary and secondary antibody incubations, samples were

630 washed according to the immunofluorescence staining procedure and then incubated with Click-iT EdU
631 reaction cocktail for 40 min, followed by DAPI counterstaining.

632 **Image acquisition and analysis**

633

634 Immunostained organ sections or whole mount retinas were imaged at high resolution with a
635 SP8 Navigator confocal microscopes fitted with 10x, 20x, or 40x objectives for confocal scanning.
636 Individual fields or tiles of large areas were acquired. All images shown are representative of the results
637 obtained for each group and experiment. Animals were dissected and processed under exactly the same
638 conditions. Comparisons of phenotypes or signal intensity were made with pictures obtained using the
639 same laser excitation and confocal scanner detection settings. Fiji/ImageJ was used to threshold, select,
640 and quantify objects in confocal micrographs. Both manual and automatic ImageJ public plugins and
641 customed Fiji macros were used for quantification.

642 **Fluorescence activated flow cytometry and sorting**

643

644 Embryonic, postnatal or adult tissues were first dissociated before fluorescence activated flow
645 cytometry or sorting (FC or FACS). Embryonic tissues were dissociated using Miltenyi Biotec Tissue
646 Dissociation Kit 2 (130-110-203) following the instructions. Postnatal and adult mouse tissues were
647 first digested for 20min at 37ºC with 2.5 mg/ml collagenase type I (Thermofisher), 2.5 mg/ml dispase
648 II (Thermofisher) and 50 **u**g/ml DNAseI (Roche).

649 Dissociated samples were filtered through a 70-µm cell strainer, and cells were centrifuged
650 (400g, 4°C for 5 min). Cell pellets were gently resuspended in blood lysis buffer (0.15 M NH_4Cl,
651 0.01M $KHCO_3$ and 0.01 M EDTA in distilled water) and incubated for 10 minutes on ice to remove
652 erythroid cells. Cells were centrifuged (400g at, 4°C for 5 min), and cell pellets were gently
653 resuspended in blocking solution (DPBS without Ca^{2+} or Mg^{2+} and containing 3% dialyzed FBS
654 (Termofisher)) and incubated at 4ºC with shaking for 20min. Cells were centrifuged (300g at 4°C for
655 5 min), resuspended and incubated for 30min at 4C with APC rat-anti-mouse CD31 and APC-CY7
656 anti-CD45 (Supplementary table 2). Cells were then centrifuged (400g, 4°C for 5 min), resuspended
657 and washed in DPBS without Ca^{2+} or Mg^{2+} and centrifuged again, and cell pellets were resuspended
658 in blocking solution. Cells were kept on ice until used for FC or FACS. DAPI (5 mg/ml) was added to
659 the cells immediately before analysis. Cells were routinely analysed in LSR Fortressa or sorted in a
660 FACS Aria Cell Sorter (BD Biosciences). BD FACS Diva V8.0.1 and Flow JO v10 was utilized for
661 FACS data collection and analysis.

662

663 **Cells isolation for transcriptomic analysis**

664

665 For qRT-PCR analysis, approximately 20.000 DAPI negative Tomato+ or YFP+ cells from dissociated
666 tissues were sorted directly to buffer RLT (RNAeasy Micro kit - Qiagen) and RNA extracted according
667 to the manufacturer instructions and stored at -80°C. This RNA was later used for qRT-PCR or RNAseq
668 analysis. For quantitative real time PCR (qRT-PCR), total RNA was retrotranscribed with the High
669 Capacity cDNA Reverse Transcription Kit with RNase Inhibitor (Thermo fisher, 4368814). cDNA was
670 preamplified with Taqman PreAmp Master Mix containing a Taqman Assay-based pre-amplification
671 pool containing a mix of the Taqman assays indicated in Supplementary Table 3. Preamplified cDNA
672 was used for qRT-PCR with the same gene specific Taqman Assays and Taqman Universal Master Mix
673 in a AB7900 thermocycler (Applied Biosystems). AB7900 software was used to retrieve and analyse
674 data.

675 For RNA-seq analysis, embryos were dissociated using Miltenyi Biotec Tissue Dissociation Kit 2 (130-
676 110-203) following the instructions. A volume of 1,2ml of dissociation solution was used per embryo
677 inside a 2ml round bottom tube. Following a 5 minutes incubation in a 37C water bath, tubes were put
678 inside a pre-warmed 50ml falcon and incubated for 25 minutes in the MACSmix Tube Rotor. After
679 cells were resuspended with a Gilson P1000 pipet for 30 times. Starting slow and increasing speed
680 gradually. To the 1.2ml of cells, 3ml of sorting buffer (10% FBS in DPBS -Ca2-Mg2-) was added and
681 this solution transferred to a 5ml syringe. This volume was pressed slowly through a small 70 µm
682 strainer to remove clumps. Each embryo gave around 30 million cells at this stage. Cells suspensions
683 were spinned at 400g for 6 minutes. Pellet was detached and ressuspended in 300µl sorting buffer
684 containing DAPI. DAPI negative, single, and live Tomato+ and YFP+ cells were sorted to eppendorf
685 tubes containing 300ul of Sorting buffer. 66k Tomato+ and 30k YFP+ cells were sorted using a 100 µm
686 Nozzle, 20 PSI and high purity scale and low flow rate (1) to preserve cell viability and decrease
687 contamination. At the end sorted cells were spinned at 500g for 5min, and resuspended in 30-40µl Cell
688 Capture Buffer (DPBS (-)Ca2+ (-)Mg2+ with 0.04%BSA). After counting cells in Countess III, two
689 independent 10x genomics ports were loaded with either 16k Tomato+ cells (90% vaibility) or 16k
690 YFP+ cells (88% viability).

691

692 **Next Generation Sequencing sample and library preparation**

693

694 Next Generation Sequencing (NGS) experiments were performed in the Genomics Unit at
695 CNIC. For scRNA-seq experiments, single cells were encapsulated into emulsion droplets using the
696 Chromium Controller (10x Genomics). scRNA-seq libraries were prepared according to the

697 manufacturer's instructions. The aimed target cell recovery for each port was 10000 cells. Generated
698 libraries were sequenced on a HiSeq4000 or NextSeq2000 (Illumina).

699

700 **Transcriptomic data analysis**

701

702 Transcriptomic data were analyzed by the CNIC Bioinformatics Unit, Alvaro Regano and Irene
703 Garcia.

704 The following pipeline was followed for scRNA-seq data processing and *in silico* cell type selection.
705 For alignment and quantification of gene expression, the reference transcriptome was built using mouse
706 genome GRCm39 and Ensembl gene build v109 (https://ftp.ensembl.org/pub/release-
707 109/fasta/mus_musculus). The WPRE-sv40pa sequences expressed in the Tomato+ and YFP+ samples
708 were added to the reference. Gene metadata were obtained from the corresponding Ensembl BioMart
709 archive. Reads from transcripts were processed, aligned and quantified using the Cell Ranger v6.1.2
710 pipeline. Single-cell analysis was based on Seurat (Hao et al., 2021) and DoubletFinder R packages.
711 Low-quality cells were filtered out using the following criteria: total counts, >1,000 and <55,000; genes
712 detected, >500 and <7,500; mitochondrial transcripts content, <15%; hemoglobin transcripts, <1%;
713 ribosomal transcripts, <35. Counts were log-normalized and scaled, followed by principal component
714 analysis (PCA) and clustering using the shared nearest-neighbors algorithm and Louvain clustering
715 (settings as defaults except for the 2,000 most variable genes, 24 principal components, and a resolution
716 of 0.35). Clusters and cells were classified based on the SingleR method (Aran et al., 2019) using
717 Blueprint ENCODE, the Human Primary Cell Atlas cell-type profile collection and a scRNASeq mouse
718 dataset from the celldex package. This identification was used to predefine the different cell types
719 present in the dataset for the analysis. Doublets were removed using DoubletFinder, using a first
720 annotation with 24 PCs, 0.25 pN and a pK of 0.05, and the second one with 10 PCs, pN0.25 and pK
721 0.05. Cells classified as Singlets were preserved. Singlets were then reclustered using 19 PCAs and a
722 clustering resolution of 0.35. Manual curation of the identified clusters was applied to confirm and
723 finetune the identity of the clusters based on scRNAseq bibliography.

724 **Copy number assay and qRT-PCR**

725 To identify the number of copies for *FlpO or Cre* expressing cassettes after transgenesis, the genomic
726 DNA was extracted from mouse tails biopsies using the phenol chloroform protocol as follows:
727 overnight digestion in 500 µL of proteinase K buffer (10 mM Tris-HCl [pH 8.0], 100 mM NaCl, 10
728 mM EDTA [pH 8.0], 0.5% sodium dodecyl sulfate, 0.25 mg/mL proteinase K) with occasional
729 vortexing. Following digestion, 250 µL of phenol and 250 µL of chloroform was added followed by
730 vigorous vortexing to ensure thorough mixing of phenol:chloroform with the sample. Samples were

731 immediately subjected to microcentrifugation at maximum speed for 5 minutes to allow separation of
732 the aqueous and organic layers. 300 µl of the aqueous top layer was removed with a 200 µl pipet, paying
733 careful attention to avoid the interface. To the 300µl of solution we added 1:10 (30µl) of sodium acetate
734 (NaAc) 3M and 2.5x (825 µl) of EtOH 100%. Then the tubes were shaken up and down 10 times to
735 precipitate the DNA. Samples were spin down at maximum speed for at least 45 minutes at 4ºC. Then
736 supernatant was removed and immediately after we added 500 µl of 70% ethanol and samples were
737 pelleted by centrifuging at max speed for 5 minutes. Pellets were re-suspended in 100µl of TE solution
738 (Tris 10mM pH=8 and EDTA 0.1mM pH=8) overnight. Next day, DNA concentrations were measured
739 in nanodrop and diluted at a final concentration of 10ng/µl.

740 For the copy number assays we performed qRT-PCR with TaqMan Universal Master Mix (TaqMan,
741 4440049) and the following probes: Tert TaqMan Copy Number Reference Assay (TaqMan probe,
742 4458369). A probe and a set of amplifying primers designed in the lab and synthetized by iDT to detect
743 the *FlpO* gene (FlpO-qPCR-F: CTGTACCAGTTCCTGTTCCTG, FlpO-qPCR-R:
744 CTTGTCTTGGTCTCGGTCAC) and qPCR FlpO Probe : TCTTGATGTCGCTGAACCTGCCG,
745 fluorophore FAM). To detect the *Cre* gene: a pre-designed Cre Assay was used (Mr00635245_cn ,
746 ThermoFisher).

747

748 With the Tert probe as a reference, the relative number of copies of the genes of interest were
749 inferred. Both Tert and FlpO/Cre probes were combined in the same reaction since they emitted two
750 different fluorophores, FAM and VIC. The qRT-PCR reactions were run in an AB7900 thermocycler
751 (Applied Biosystems).

752

753 **Statistical analysis and Reproducibility**

754

755 All bar graphs show mean ± s.d. Experiments were repeated with independent animals.
756 Comparisons between two groups of samples with a Gaussian distribution were carried out by unpaired
757 two-tailed Student *t*-test. Comparisons among more than two groups were made by one-way ANOVA
758 followed by multiple comparison tests. All calculations were done in Excel, and final datapoints were
759 analyzed and represented with GraphPad Prism. No randomization or blinding was used, and animals
760 or tissues were selected for analysis based on their genotype, the detected Cre/FlpO/Dre-dependent
761 recombination frequency, and the quality of multiplex immunostaining. Sample sizes were chosen
762 according to the observed statistical variation and published protocols.

763

764

Data availability

RNA-seq data can be viewed at the Gene Expression Omnibus (GEO) under accession numbers GSEXXXX. Instructions and code to reproduce all scRNA-seq results can be found at https://github.com/RuiBenedito/Benedito_Lab. Unprocessed original photos of the data are available upon request. All other data supporting the findings in this study are included in the main article and associated files.

Acknowledgments

Research in the Benedito laboratory was supported by the European Research Council (ERC) Starting Grants AngioGenesHD (638028) and Consolidator Grant AngioUnrestUHD (101001814), the Ministerio de Ciencia y Innovación (SAF2017-89299-P and PID2020-120252RB-I00) and "la Caixa" Banking Foundation (project code HR19-00120 and HR22-00316 AngioHeart). The CNIC is supported by the Instituto de Salud Carlos III (ISCIII), the Ministerio de Ciencia e Innovación (MCIN) and the Pro CNIC Foundation, and is a Severo Ochoa Center of Excellence (grant CEX2020-001041-S funded by MICIN/AEI/10.13039/501100011033).

Microscopy experiments were performed at Microscopy and Dynamic Image Unit, CNIC, ICTS-ReDib, co-funded by MCIN/AEI /10.13039/501100011033 and FEDER "Una manera de hacer Europa" (#ICTS-2018-04-CNIC-16).

I.G.-G. was supported by a PhD fellowship from Fundación La Caixa (CX-SO-16-1). A.R. was supported by The Youth Employment Initiative (YEI) PEJD-2019-PRE/BMD-16990. L.G.-O. was supported by the Spanish Ministry of Economy and Competitiveness (PRE2018-085283). S. G. was supported by Juan de la Cierva Fellowship (FJC2020-044237-I). M.F.-C. was supported by PhD fellowships from Fundación La Caixa (CX_E-2015-01).

We thank S. Bartlett (CNIC) for English editing; the members of the CNIC Transgenesis, Microscopy, Genomics, Citometry and Bioinformatic units. We also thank F. Alt (Boston Children's Hospital - Harvard Medical School), T. Honjo (Kyoto University Institute for Advanced Studies), F. Radtke (Swiss Institute for Experimental Cancer Research), R. H. Adams (Max Planck Institute for Molecular Biomedicine) and R. De Pinho (MD Anderson Cancer Center) for sharing the *Myc* ^{floxed}, *Rbpj* ^{floxed}, *Notch1*^{floxed}, *Cdh5(PAC)-creERT and Foxos1/3/4*^{floxed} mice respectively. We also thank the master students Joan Marc Arbonés and Alejandro Rivera Sánchez for their work on *iFlpMosaics*.

797 **Author contributions statement**

798

799 I.G-G. and R.B. designed most of the experiments, interpreted results, assembled figures and wrote
800 the manuscript. R.B. designed all DNA vectors. I.G-G. did most of the DNA engineering (cloning),
801 CRISPR-Cas9 genome targeting and executed the large majority of the animal experiments, confocal
802 microscopy and FACS analysis. Mice were generated by the CNIC transgenesis unit. S.G. developed
803 new methods for *iFlpMosaics* induction, tissues immunostaining and multispectral microscopy
804 imaging, executed animal experiments, image analysis and interpreted results. L.G-O, W.L., I.Z. and
805 M.F-C. performed some animals experiments, FACS, histology and confocal imaging. I.G-G and A.R
806 analysed scRNA-seq data. A.R. cloned and validated the *iFlp/Dre*^{Progenitor} allele. S.F.R. did image
807 quantifications in Fiji, graphpad, text and figures editing and figures assembly. M.L, M.S.S-M, A.G.-C,
808 F.L. and V.C-G gave general technical assistance with experiments and genotyped the mouse colonies.
809 All authors approved the final version of the manuscript.

810

811 **Competing interests statement**

812 The authors declare no competing interests.

813

814

815

816

817

818

819

820

821

822

823

824

825 **Figure legends:**

826 **Figure 1: *iFlpMosaics* allow efficient and ratiometric labelling of mutant and wildtype cells. a,**
827 Schematic showing a standard Cre-reporter and how it may recombine and label cells without any
828 floxed gene (G) deleted (false positives). Non-recombined cells can also have the gene deleted (false
829 negatives). **b,** Different recombination efficiencies of several Cre-reporters, despite all localizing to the
830 *Rosa26* locus and having a similar genetic distance between LoxP sites. **c,d,** Cre-reporters only
831 accurately report recombination of themselves, not of other floxed alleles (reporters), particularly at low
832 doses of tamoxifen. **e,** Schematic of the novel R26-*iFlp*$^{MTomato\text{-}Cre/MYFP}$ allele, where Flpo/FlpOERT2-
833 induced recombination of the mutually exclusive FRTF3 and FT5T2 sites leads to one of two possible
834 outcomes (see also Sup. Fig. 1). Cells expressing MTomato and Cre (mutant) or MYFP (wildtype). The
835 induction leads to the ratiometric proportion of around 65%MTom+:35%MYFP+. **f**, Tg-*iFlp*$^{MTomato\text{-}H2B\text{-}}$
836 $^{GFP\text{-}Cre/MYFP\text{-}H2B\text{-}Cherry\text{-}FlpO}$ allele and confocal micrographs showing the full spectral separation of the 4
837 fluorescent labels expressed in mutant and wildtype cells. **g,** In a wildtype background, the initial
838 ratiometric proportions between MTomato+ cells and MYFP+ cells are maintained through
839 embryogenesis to postnatal stages, indicating lack of toxicity of Cre in MTomato+ cells. **h**, Comparison
840 of MTomato intensity and Cre expression in cells of R26-*iFlp*$^{MTomato\text{-}Cre/MYFP}$ and Tg(*iSure-Cre*) mice. **i,**
841 Efficient recombination of the Cre-reporter *Rosa26*$^{\text{-}LSL\text{-}YFP}$ in MTomato+ cells (white arrowheads) after
842 induction of the R26-*iFlp*$^{MTomato\text{-}Cre/MYFP}$ allele by *Apln-FlpO*. Few cells are false positives (red arrows).
843 FACS data of the same animals livers and related chart. **j,** Combination of the *iFlp*$^{MTomato\text{-}Cre/MYFP}$ allele
844 with other floxed genes leads to very significant deletion of these in MTomato+ cells. **k,** Induction of
845 *iFlp*$^{MTomato\text{-}Cre/MYFP}$ in the *Rbpj* floxed background, a gene known to be essential for arterial development,
846 results in only 3.5% Tomato-2A-Cre+ cells in arteries (A), versus 96% in veins (v) and capillaries. Data
847 are presented as mean values +/- SD. For statistics see Source Data File 1. Scale bars are 50µm.
848

849 **Figure2: Generation of ubiquitous and tissue-specific FlpoERT2 mouse lines. a,** Recombination of
850 the *iFlp*$^{MTomato\text{-}Cre/MYP}$ mosaic mouse lines induced by the published *R26*$^{CAG\text{-}FlpoERT2}$, led to reduced
851 recombination efficiency at embryonic and postnatal stages and in adult organs. **b,** Schematic of novel
852 *Tg(Ins-CAG-FlpoERT2*) alleles containing optimized DNA elements in order to enhance FlpOERT2
853 expression. **c,** Comparison of FlpO copy number by genomic DNA qRT-PCR. **d-g** Comparison by
854 FACS and histology of the recombination efficiency among the different FlpOERT2-expressing mouse
855 lines/founders at embryonic, postnatal and adult stages. Fold change is indicated for the most
856 significant. **h,** Schematic of the generation of novel endothelial-specific *Cdh5-FlpoERT2*-expressing
857 mouse lines from the published *Cdh5-CreERT2* mouse line by Crispr/Cas9 targeting. **i,** Comparison of
858 FlpO and Cre copy number by genomic DNA qRT-PCR. **j,** Recombination efficiency of Founder #1 of
859 the newly generated *Tg(Cdh5-FlpoERT2)* mouse line in embryonic, postnatal and adult tissues. Data
860 are presented as mean values +/- SD. For statistics see Source Data File 1. Scale bars are 100µm.

861
862
863 **Figure3: Ratiometric iFlpMosaics allow the high-throughput assessment of a gene cell-**
864 **autonomous function. a,b,** *iFlp*$^{MTomato\text{-}Cre/MYP}$ mosaics were induced with *Apln-FlpO* (recombines
865 endothelial and derived hematopoietic cells at E9.5) in a control/wildtype and Myc floxed background,
866 and tissues analysed at P7. FACS data of CD31+ (ECs) and CD45+ (Blood) cells shows that *Myc*
867 deletion (in MTomato+ cells) leads to a competitive disadvantage, especially in blood cells. Absolute
868 fold change indicated in red. **c,** When *iFlp*$^{MTomato\text{-}Cre/MYFP}$ mosaics are induced in most embryonic cells
869 with *ACTB:FlpE*, analysis of other organs cell types (CD31-CD45-) reveals that *Myc* is necessary for
870 liver, but not lung or heart cells development. **d,** *iFlp*$^{MTomato\text{-}Cre/MYP}$ mosaics were combined with *Tg(Ins-*
871 *CAG-FlpOERT2)* on a control/wildtype and *Foxo1/3/4* floxed background and tamoxifen injected at P1
872 to induce recombination in all cell types. Liver, lung and heart cells were analysed at P15 by FACS.
873 *Foxo1/3/4* deletion (in MTomato+ cells) increased the proliferation of heart cells, but not liver or lung
874 cells. **e,** Representative confocal micrographs of control and *Foxo1/3/4* mosaic P6 and P15 retinas of
875 animals induced at P1. Chart with ratiometric analysis of retina immunostainings for Tomato, YFP and
876 ERG (labels ECs nuclei) showing that *Foxo1/3/4*^{KO} ECs have a competitive advantage. Data are
877 presented as mean values +/- SD. For statistics see Source Data File 1. Scale bars are 100µm.
878
879 **Figure 4: Combining *iFlp-Mosaic* with *iFlp*^{Chromatin} for higher single-cell clonal resolution. a,**
880 Representative confocal micrograph of adult liver sections of mice carrying the *Tg(Ins-CAG-*
881 *FlpoERT2), iFlp*$^{MTomato\text{-}Cre/MYFP}$ and *Rosa26-iChr2-Mosaic (iCre*$^{H2B\text{-}Cherry/GFP/Cerulean}$) alleles. Combination
882 of these membrane and nuclear reporter alleles allow up to 3 different mutant and 1 wildtype cell
883 barcodes (labelling). Note that binucleated (2x2n) or polyploid (4n) hepatocytes can have more
884 multispectral barcodes. **b,** Representative confocal micrograph of a P7 retina from an animal containing
885 the *Tg(Ins-CAG-FlpOERT2)* and the new *iFlp*^{Chromatin} nuclear reporter allele (for similar DNA elements
886 explanation see Sup. Fig.4c) induced at P1 with 4-OHT. Bar shows ratiometric frequency of each
887 nuclear/H2B+ fluorescent marker. **c,** Representative confocal micrograph of the indicated adult organ
888 sections of animals carrying the *iFlp*^{Chromatin} and *Tg(Ins-CAG-FlpoERT2)* alleles. Mononucleated diploid
889 cells (kidney and lung) express only 1 of 3 possible nuclei/chromatin markers, while multinucleated or
890 polyploid cells (hepatocytes and cardiomyocytes) can express a combination of 2 or 3 possible markers
891 (6 possible chromatin barcodes in total). **d,** Recombination and cell barcoding possibilities in animals
892 carrying the indicated alleles. A representative P7 retina confocal micrograph showing that both
893 wildtype and mutant cells can be labelled in 4 different ways, which significantly increases single cell
894 clonal resolution. On the right is shown an example of how a Fiji image analysis script automatically
895 detects, segments, and pseudocolor the nuclei of dual-labelled (nuclei and membrane) cells. **e,**
896 Recombination and diploid cell barcoding possibilities in animals carrying the indicated alleles. A
897 representative confocal micrograph of an adult liver, collected 2 weeks after tamoxifen induction, showing that

898 mutant hepatocytes can be labelled with up to 16 different fluorescent barcodes, depending on whether these
899 are mononucleated/diploid or multinucleated/polyploid. Also wildtype hepatocytes can have up to 8 different
900 fluorescent barcodes (only 6 shown). Scale bars are 100µm.

901

902 **Figure 5: High-resolution *iFlpMosaics* reveals the impact of genetic mutations in single cell clonal**
903 **dynamics. a,** Quantification of Ki67+ (in cycle) or EdU+ (S-phase) cells in P1, P7 and P20 livers. **b,**
904 Schematic of the indicated alleles combined in a single animal and how they can be used to fluorescently
905 barcode and track single mutant and wildtype cells clonal expansion from P1 to P20. Representative
906 confocal micrographs of P20 livers (from animals induced with 4-OHT at P1) with different
907 recombination frequencies are shown (see also Sup. Fig. 5). **c,** Recombination and fluorescent
908 barcoding density did not affect the clonal quantification. **d,** Liver weight increases 2.9 fold from P1
909 and P20. **e,** Quantification of MYFP+ (Myc^{WT}) and MTomato+ (Myc^{KO}) clone size frequency showing
910 that Myc^{KO} hepatocytes divide less. **f,** Chart depicting the normalized expansion of Myc^{WT} and Myc^{KO}
911 hepatocytes over the same period of 20 days. **g,** Representative confocal micrographs of P20 pancreas
912 from control and *Myc floxed* mice having the indicated *iFlpMosaic* alleles. Right panels correspond to
913 inverted LUT images depicting the clones mapping (by Fiji image analysis scripts) according to their
914 dual color code. **h,** Quantification of MYFP+ (Myc^{WT}) and MTomato+ (Myc^{KO}) clone size frequency
915 showing that Myc^{KO} pancreatic cells divide less. **i,** Chart depicting the normalized expansion of Myc^{WT}
916 and Myc^{KO} pancreatic cells over the same period of 20 days. **j,** Log2 ratio between Tom+ and YFP+
917 cells in control and *Myc floxed* pancreas showing a 3.7 fold loss of MTomato+ (Myc^{KO}) cells over 20
918 days. **k,** Representative confocal micrographs of adult livers from control and *Myc floxed* mice having
919 the indicated *iFlpMosaic and* $iCre^{Mb2\text{-}Mosaic}$ alleles induced 14 days before tissue collection. Right panels
920 correspond to automatic mapping of clones, using Fiji image analysis scripts, according to their
921 fluorescent barcode. Note the loss of MTomato+ cells in the Myc floxed background. **l,** Clone size
922 showing that wildtype hepatocytes rarely divide or expand over a period of 2 weeks. **m,** Quantification
923 of wildtype MYFP+ and MTomato+ hepatocyte clone frequency reveals no impact of Cre expression
924 in MTomato+ cells. Note the difference between diploid, mononucleated, polynucleated and polyploid
925 cells. **n,** Quantification of the percentage of YFP+ and Tomato+ clones that are proliferative (composed
926 by more than 1 cell) and non-proliferative. No major difference observed between both wildtype
927 populations. **o,** Log2 ratio of the Tom+ and YFP+ cells frequency in control and adult *Myc floxed* livers,
928 showing that a big fraction of Myc^{KO} cells are lost over 2 weeks. **p,** Among the surviving Myc^{KO} cells,
929 the frequency of non-proliferative binucleated cells increases and the frequency of proliferative
930 mononucleated cells decreases. **q,** Quantification of the percentage of YFP+ (Myc^{WT}) and Tomato+
931 (Myc^{KO}) clones that are proliferative and non-proliferative. Loss of *Myc* reduces the frequency of
932 proliferative clones.

933 **Figure 6: *iFlp/Dre^{Progenitor}* enables the induction of genetic mosaics in the progeny of single cells.**
934 **a,** Schematic of the *iFlp/Dre^{Progenitor}* DNA construct used to generate mice by transgenesis. **b**,
935 CRISPR-Cas9 assisted targeting of the *iFlp/Dre^{Progenitor}* donor DNA on an existing *Tg(Ins-CAG-*
936 *FlpOERT2)^{F4}* multicopy allele. **c,** Generation of *Tg(Ins-CAG-DreERT2)* by CRISPR-Cas9 mediated
937 replacement of FlpO by Dre in the existing *Tg(Ins-CAG-FlpOERT2)^{F4}* allele. **d**, Schematic of the
938 genetic cascade induced in animals containing the indicated alleles. After tamoxifen induction of
939 FlpOERT2 or DreERT2, the *iFlp/Dre^{Progenitor}* allele is recombined driving expression of the nuclei
940 marker H2B-V5, the surface marker truncated human CD2 (hCD2) and FlpO. FlpO is a relatively
941 weak recombinase, that needs to be expressed and accumulate in the cell before it recombines the
942 *iFlp$^{MTomato-Cre/MYFP}$* allele. This delay results in recombination in the progeny of a single progenitor cell.
943 **e**,**f**, In animals lacking the *iFlp/Dre^{Progenitor}* allele, most single cell derived clones are formed by only
944 one type of cell (MTomato+ or MYFP+). With the *iFlp/Dre^{Progenitor}* allele is possible to induce clones
945 formed by mutant (MTomato+) and wildtype (MYFP+) cells derived from single progenitor cells (see
946 also Sup. Fig. 6). **g**, Retinas confocal micrographs showing that the *iFlp/Dre^{Progenitor}* allele increases
947 significantly the frequency of recombination of the *iFlp$^{MTomato-Cre/MYFP}$* allele (induced at P3 and
948 collected at P7), enabling high frequency genetic mosaics with the weaker *Cdh5-FlpOERT2* line
949 (expressed only in Cdh5+ ECs). H2B-V5 labels the nuclei of cells recombining/expressing the
950 *iFlp/Dre^{Progenitor}* allele. **h**, FACS plots showing that the *iFlp/Dre^{Progenitor}* allele increases significantly
951 the frequency of recombination of the *iFlp$^{MTomato-Cre/MYFP}$* allele when combined with the *Tg(Ins-CAG-*
952 *FlpOERT2)* allele.
953 **i**, Retinas confocal micrographs showing that when the new *Tg(Ins-CAG-DreERT2)* line is combined
954 with the *iFlp/Dre^{Progenitor}* allele, recombination of the *iFlp$^{MTomato-Cre/MYFP}$* allele is also much more
955 frequent. H2B-V5 labels the nuclei of cells recombining/expressing the *iFlp/Dre^{Progenitor}* allele.
956
957 **Figure 7 : Combining single cell RNA-seq with ratiometric *iFlp^{Mosaics}* to uncover cell-autonomous**
958 **gene function. a,** Schematic of the induction of embryos having the indicated alleles at E9.5 and
959 collection of cells at E13.5 by FACS for scRNA-seq. **b**, Umaps showing the spatial distribution of the
960 *Rbpj^{KO}* (MTomato+) and *Rbpj^{Wt}* (MYFP+) cells and the different clusters they form. On the right, dot
961 plot showing the top markers used for the identification of the major cell types. **c**, Dot plot showing the
962 frequency and amplitude of expression for *Rbpj,* the canonical Notch target *Hes1*, and the G2/M phase
963 (proliferation) marker *MKi67* among wildtype (MYFP+) and mutant (MTomato-2A-Cre+) cells. Note
964 that *Rbpj* deletion only removes exons 6 and 7, leaving the 3´mRNA intact. However, this truncated
965 mRNA is less stable and less detectable after deletion. **d**,**e**, Histobars and Umap showing that mosaic
966 deletion of *Rbpj* (MTomato+ cells) changes the relative proportion of different cell types. **f-r**, Umaps
967 with the cell-type specific subclusters, top deregulated marker genes, and gene set enrichment analysis
968 charts showing how *Rbpj* deletion changes the frequency, differentiation and biology of the indicated
969 cell types.

970 **Supplementary Figure 1: *iFlpMosaics* are not toxic or leaky.**

971 **a, b,** Schematic of the novel Rosa26-*iFlp*$^{MTomato\text{-}Cre/MYFP}$ and Tg-*iFlp*$^{MTomato\text{-}H2B\text{-}GFP\text{-}Cre/MYFP\text{-}H2B\text{-}Cherry\text{-}FlpO}$
972 alleles, the genetic distances between the FRT sites pairs (mutually exclusive), and expected outcomes
973 after FlpO/FlpOERT2 recombination. **c, d** Mouse ES cells used to generate Rosa26-*iFlp*$^{MTomato\text{-}Cre/MYFP}$
974 mice were transfected with FlpO expressing plasmids, and analysed by confocal microscopy or FACS
975 3 days after. **e-g**, Frequency of recombination/expression detected in ES cells and ECs derived from
976 embryoid bodies (EBs) by microscopy. **h**, Relative frequency of MTomato-2A-Cre+ and MYFP+
977 cells does not change over time in both ES cells (in vitro) and in blood (in vivo), showing that the
978 permanent expression of Cre is not toxic to the cells. **i**, Combination of the standard *Rosa26-LSL-YFP*
979 allele with *iFlpMosaics* alleles allow determination of FlpO versus Cre-dependent leakiness by FACS
980 analysis of adult organs. FlpO leakiness was not detected (0% Tomato+ cells), and Cre-non-self-
981 leakiness (only detectable with the additional *Rosa26-LSL-YFP* allele) was only observed in a very
982 small fraction of cells from animals carrying the Tg-*iFlp*$^{MTomato\text{-}H2B\text{-}GFP\text{-}Cre/MYFP\text{-}H2B\text{-}Cherry\text{-}FlpO}$ allele. Not
983 in animals having the Rosa26-*iFlp*$^{MTomato\text{-}Cre/MYFP}$ allele.

984 **Supplementary Figure 2: Validation of *iFlpMosaics* for ratiometric quantitative gene function**
985 **analysis. a,** Representative confocal micrograph of P6 retinas of *Rbpj floxed* mice carrying the
986 *iFlp*$^{MTomato\text{-}Cre/MYFP}$ and *Apln-FlpO* alleles. *Apln* is an X-chromosome gene (mosaicly expressed in
987 females), expressed at the angiogenic front of growing vessels, recombining ECs that later form the
988 entire vasculature. It also recombines non-endothelial (ERG negative) cells in the retina. Right panel
989 showing ERG signal segmentation (EC nuclei), with nuclei belonging to Tomato+ (*Rbpj*^{KO}) cells or
990 YFP+ (*Rbpj*^{WT}) cells outlined in red or green, respectively. Grey nuclei are of ERG+ objects of non-
991 recombined cells. Dashed white lines show limits of leading edge (LE), angiogenic front (AF) and
992 mature area (MA). Chart depicting the log2 of the ratio between Tomato+ and YFP+ ECs in each of the
993 retinal regions, highlighting the enrichment of *Rbpj*^{KO} cells in the LE and AF, suggesting a role for this
994 gene in cell migration. **b,** Representative confocal micrograph of P6 retinas of *Rbpj floxed* mice carrying
995 the *iFlp*$^{MTomato\text{-}H2BGFP\text{-}Cre/MYFP\text{-}H2BCherry}$ and *Apln-FlpO* alleles, which also allows the nuclear labelling of
996 *Rbpj*^{KO} (H2B-GFP+) and *Rbpj*^{Wt} (H2B-Cherry+) cells, which is more convenient for cell object
997 segmentation and quantification of nuclear-specific proteins, such as the proliferation and cell cycle
998 arrest markers Ki67 and p21. Scale bars 150µm.

999 **Supplementary Figure 3: Comparative analysis of recombination efficiency of FlpOERT2 mouse**
1000 **lines. a-d,** Representative FACs plots of different adult organs showing YFP+ and Tomato+ cell
1001 frequency obtained from mice carrying the *iFlp*$^{MTomato\text{-}Cre/MYFP}$ allele combined with either the published
1002 *R26*$^{CAG\text{-}FlpoERT2}$ or the newly generated *Tg(Ins-CAG-FlpoERT2)*^{F2} allele. **e,** Chart showing the lack of
1003 leakiness of the *Tg(Ins-CAG-FlpoERT2)*^{F2} allele. In the absence of tamoxifen the *iFlp*$^{MTomato\text{-}Cre/MYFP}$
1004 allele is not recombined.

1005 **Supplementary Figure 4: Ratiometric iFlpMosaics show that *Myc^{KO}* cells have a stronger**
1006 **competitive disadvantage in blood than ECs. a,b,** Representative FACS plots showing that in both
1007 the heart and the lung CD45+ blood cells are much more affected by *Myc* deletion than CD31+ ECs. **c**,
1008 Schematic of *iChr2-Mosaic* or *iCre$^{H2B\text{-}Cherry/GFP/Cerulean}$* construct, targeted in the Rosa26 locus and having
1009 4 insulator (INS) sequences and the strong and ubiquituous CAG enhancer/promoter. N-PhiMut codes
1010 for a non-fluorescent nuclei marker protein detectable with an antibody. It is expressed before Cre
1011 recombination. After Cre-mediated recombination between compatible pairs of LoxP sites, only one of
1012 the 3 possible fluorescent proteins will be expressed. WPRE is the woodchuck hepatitis virus post-
1013 transcriptional regulatory element to enhance transgene expression. pA is the Sv40 polyA to terminate
1014 transcription.

1015 **Supplementary Figure 5: Mapping the clonal expansion of single mutant and wildtype cells with**
1016 ***iFlpMosaics*. a,b,** Representative confocal images (large tile scans), at low magnification, of entire P20
1017 liver sections of mice carrying the indicated alleles. Recombination of the reporter alleles was induced
1018 at P1 and resulted in different recombination frequencies. Right panels show automatic image
1019 processing results using Fiji scripts, that generate spatial maps of dual-labelled clones of cells (with
1020 membrane and nuclear labelling). The bigger the circle, the bigger the clone. **c,** Quantification and
1021 representative confocal micrographs of proliferative pancreatic cells (Ki67+ in cycle or EdU+ in s-
1022 phase) at different postnatal stages. **d,** Quantification and representative confocal micrograph of
1023 Ki67+/DAPI+ cells in the adult liver. **e,** Representative confocal micrographs of adult liver sections
1024 from control and *Myc floxed* mice combined with the indicated alleles. Left panels show endogenous
1025 fluorescent signals from the reporter alleles and left panels show sections from the same mice
1026 immunostained with antibodies that bind to DsRed (detects MTomato and H2B-Cherry), or GFP
1027 (detects MYFP and H2B-GFP) or the HA epitope (detects MTFP1 and H2B-Cerulean). Right panels
1028 show automatic image processing results using Fiji scripts, that generate spatial maps of dual-labelled
1029 clones of cells (with membrane and nuclear labelling) reveal hepatocytes ploidy and clone size. Chart
1030 showing that in control mice, MYFP+ (WT) and MTomato+ (WT) diploid cells occur in similar
1031 proportions, while in *Myc* floxed mutants, MTomato+ (*Myc^{KO}*) diploid cells are more frequently
1032 binucleated and give rise to less 2-cell mononucleated clones than MYFP+ (*Myc^{WT}*) cells.

1033

1034 **Supplementary Figure 6: *iFlp/Dre^{Progenitor}* enables the induction of genetic mosaics from a single**
1035 **progenitor cell. a,** Representative confocal micrograph of a P7 retina of an animals carrying the
1036 indicated alleles and induced with 4-OHT at P3. After induction of the ***iFlp/Dre^{Progenitor}*** allele, cells will
1037 express the nuclei marker H2B-V5 and FlpO. FlpO will after some time and cell division recombine
1038 the *iFlp$^{MTomato\text{-}Cre/MYFP}$* allele generating MYFP+ and MTomato+ progeny cells derived from a single
1039 initial recombination event.

Supplementary Figure 7: Single cell RNA-seq analysis combined with ratiometric iFlpMosaics uncovers cell-autonomous gene function in diverse cell types.

a, UMAPs and barplots showing the identified clusters and their frequencies among YFP+ (*Rbpj*^{WT}) and Tomato+ (*Rbpj*^{KO}) cells. **b,** Dot plots showing the frequency (size) and expression level (intensity of color) for the top cluster marker genes. **c,** Top differentially expressed genes per cluster between YFP+ (*Rbpj*^{WT}) and Tomato+ (*Rbpj*^{KO}) cells. For most is also shown the expression of *Rbpj*, its canonical target *Hes1* and the proliferation markers *Ki67* (G2/M) and *Cdkn1a* (arrested cells). **d,** Gene set enrichment analysis (GSEA) pathways with their normalized enrichment score. For some cell types there are no differentially expressed genes or pathways.

1075 **References**

1076

1077 Aran, D., Looney, A.P., Liu, L., Wu, E., Fong, V., Hsu, A., Chak, S., Naikawadi, R.P., Wolters, P.J., Abate,
1078 A.R., et al. (2019). Reference-based analysis of lung single-cell sequencing reveals a
1079 transitional profibrotic macrophage. Nat Immunol *20*, 163-172. 10.1038/s41590-018-0276-y.
1080 Cai, D., Cohen, K.B., Luo, T., Lichtman, J.W., and Sanes, J.R. (2013). Improved tools for the Brainbow
1081 toolbox. Nature methods *10*, 540-547.
1082 Claveria, C., Giovinazzo, G., Sierra, R., and Torres, M. (2013). Myc-driven endogenous cell
1083 competition in the early mammalian embryo. Nature *500*, 39-44. 10.1038/nature12389.
1084 Contreras, X., Amberg, N., Davaatseren, A., Hansen, A.H., Sonntag, J., Andersen, L., Bernthaler, T.,
1085 Streicher, C., Heger, A., Johnson, R.L., et al. (2021). A genome-wide library of MADM mice for
1086 single-cell genetic mosaic analysis. Cell reports *35*, 109274. 10.1016/j.celrep.2021.109274.
1087 de Alboran, I.M., O'Hagan, R.C., Gartner, F., Malynn, B., Davidson, L., Rickert, R., Rajewsky, K.,
1088 DePinho, R.A., and Alt, F.W. (2001). Analysis of C-MYC function in normal cells via
1089 conditional gene-targeted mutation. Immunity *14*, 45-55.
1090 Dharaneeswaran, H., Abid, M.R., Yuan, L., Dupuis, D., Beeler, D., Spokes, K.C., Janes, L., Sciuto, T.,
1091 Kang, P.M., Jaminet, S.S., et al. (2014). FOXO1-mediated activation of Akt plays a critical role
1092 in vascular homeostasis. Circ Res *115*, 238-251. 10.1161/CIRCRESAHA.115.303227.
1093 Eijkelenboom, A., and Burgering, B.M. (2013). FOXOs: signalling integrators for homeostasis
1094 maintenance. Nat Rev Mol Cell Biol *14*, 83-97. 10.1038/nrm3507.
1095 Ema, M., Takahashi, S., and Rossant, J. (2006). Deletion of the selection cassette, but not cis-acting
1096 elements, in targeted Flk1-lacZ allele reveals Flk1 expression in multipotent mesodermal
1097 progenitors. Blood *107*, 111-117. 10.1182/blood-2005-05-1970.
1098 Fernandez-Chacon, M., Casquero-Garcia, V., Luo, W., Francesca Lunella, F., Ferreira Rocha, S., Del
1099 Olmo-Cabrera, S., and Benedito, R. (2019). iSuRe-Cre is a genetic tool to reliably induce and
1100 report Cre-dependent genetic modifications. Nature communications *10*, 2262.
1101 10.1038/s41467-019-10239-4.
1102 Han, H., Tanigaki, K., Yamamoto, N., Kuroda, K., Yoshimoto, M., Nakahata, T., Ikuta, K., and Honjo, T.
1103 (2002). Inducible gene knockout of transcription factor recombination signal binding protein-
1104 J reveals its essential role in T versus B lineage decision. Int Immunol *14*, 637-645.
1105 Hansen, A.H., and Hippenmeyer, S. (2020). Non-Cell-Autonomous Mechanisms in Radial Projection
1106 Neuron Migration in the Developing Cerebral Cortex. Front Cell Dev Biol *8*, 574382.
1107 10.3389/fcell.2020.574382.
1108 Hansen, A.H., Pauler, F.M., Riedl, M., Streicher, C., Heger, A., Laukoter, S., Sommer, C., Nicolas, A.,
1109 Hof, B., Tsai, L.H., et al. (2022). Tissue-Wide Effects Override Cell-Intrinsic Gene Function in
1110 Radial Neuron Migration. Oxford Open Neuroscience *1*. 10.1093/oons/kvac009.
1111 Hao, Y., Hao, S., Andersen-Nissen, E., Mauck, W.M., 3rd, Zheng, S., Butler, A., Lee, M.J., Wilk, A.J.,
1112 Darby, C., Zager, M., et al. (2021). Integrated analysis of multimodal single-cell data. Cell *184*,
1113 3573-3587 e3529. 10.1016/j.cell.2021.04.048.
1114 He, C., Hu, H., Braren, R., Fong, S.-Y., Trumpp, A., Carlson, T.R., and Wang, R.A. (2008). c-myc in the
1115 hematopoietic lineage is crucial for its angiogenic function in the mouse embryo.
1116 Development *135*, 2467-2477. 10.1242/dev.020131.
1117 He, L., Pu, W., Liu, X., Zhang, Z., Han, M., Li, Y., Huang, X., Han, X., Li, Y., Liu, K., et al. (2021).
1118 Proliferation tracing reveals regional hepatocyte generation in liver homeostasis and repair.
1119 Science *371*, eabc4346. doi:10.1126/science.abc4346.
1120 Hunter, N.L., Awatramani, R.B., Farley, F.W., and Dymecki, S.M. (2005). Ligand-activated Flpe for
1121 temporally regulated gene modifications. Genesis *41*, 99-109. 10.1002/gene.20101.
1122 Knoepfler, P.S., Cheng, P.F., and Eisenman, R.N. (2002). N-myc is essential during neurogenesis for
1123 the rapid expansion of progenitor cell populations and the inhibition of neuronal
1124 differentiation. Genes Dev *16*, 2699-2712. 10.1101/gad.1021202.

1125 Kranz, A., Fu, J., Duerschke, K., Weidlich, S., Naumann, R., Stewart, A.F., and Anastassiadis, K. (2010).
1126 An improved Flp deleter mouse in C57Bl/6 based on Flpo recombinase. Genesis *48*, 512-520.
1127 10.1002/dvg.20641.
1128 Lao, Z., Raju, G.P., Bai, C.B., and Joyner, A.L. (2012). MASTR: a technique for mosaic mutant analysis
1129 with spatial and temporal control of recombination using conditional floxed alleles in mice.
1130 Cell reports *2*, 386-396. 10.1016/j.celrep.2012.07.004.
1131 Liu, J., Willet, S.G., Bankaitis, E.D., Xu, Y., Wright, C.V., and Gu, G. (2013). Non-parallel recombination
1132 limits cre-loxP-based reporters as precise indicators of conditional genetic manipulation.
1133 Genesis *51*, 436-442. 10.1002/dvg.22384.
1134 Livet, J., Weissman, T.A., Kang, H., Draft, R.W., Lu, J., Bennis, R.A., Sanes, J.R., and Lichtman, J.W.
1135 (2007). Transgenic strategies for combinatorial expression of fluorescent proteins in the
1136 nervous system. Nature *450*, 56-62. nature06293 [pii]

1137 10.1038/nature06293.
1138 Loonstra, A., Vooijs, M., Beverloo, H.B., Allak, B.A., van Drunen, E., Kanaar, R., Berns, A., and Jonkers,
1139 J. (2001). Growth inhibition and DNA damage induced by Cre recombinase in mammalian
1140 cells. Proc Natl Acad Sci U S A *98*, 9209-9214. 10.1073/pnas.161269798.
1141 Luo, W., Garcia-Gonzalez, I., Fernández-Chacón, M., Casquero-Garcia, V., Sanchez-Muñoz, M.S.,
1142 Mühleder, S., Garcia-Ortega, L., Andrade, J., Potente, M., and Benedito, R. (2021).
1143 Arterialization requires the timely suppression of cell growth. Nature *589*, 437-441.
1144 10.1038/s41586-020-3018-x.
1145 Madisen, L., Zwingman, T.A., Sunkin, S.M., Oh, S.W., Zariwala, H.A., Gu, H., Ng, L.L., Palmiter, R.D.,
1146 Hawrylycz, M.J., Jones, A.R., et al. (2010). A robust and high-throughput Cre reporting and
1147 characterization system for the whole mouse brain. Nat Neurosci *13*, 133-140.
1148 10.1038/nn.2467.
1149 Munoz-Martin, N., Sierra, R., Schimmang, T., Villa Del Campo, C., and Torres, M. (2019). Myc is
1150 dispensable for cardiomyocyte development but rescues Mycn-deficient hearts through
1151 functional replacement and cell competition. Development *146*. 10.1242/dev.170753.
1152 Naiche, L.A., and Papaioannou, V.E. (2007). Cre activity causes widespread apoptosis and lethal
1153 anemia during embryonic development. Genesis *45*, 768-775. 10.1002/dvg.20353.
1154 Paik, J.H., Kollipara, R., Chu, G., Ji, H., Xiao, Y., Ding, Z., Miao, L., Tothova, Z., Horner, J.W., Carrasco,
1155 D.R., et al. (2007). FoxOs are lineage-restricted redundant tumor suppressors and regulate
1156 endothelial cell homeostasis. Cell *128*, 309-323. 10.1016/j.cell.2006.12.029.
1157 Pontes-Quero, S., Fernández-Chacón, M., Luo, W., Lunella, F.F., Casquero-Garcia, V., Garcia-
1158 Gonzalez, I., Hermoso, A., Rocha, S.F., Bansal, M., and Benedito, R. (2019). High mitogenic
1159 stimulation arrests angiogenesis. Nature communications *10*, 2016. 10.1038/s41467-019-
1160 09875-7.
1161 Pontes-Quero, S., Heredia, L., Casquero-Garcia, V., Fernandez-Chacon, M., Luo, W., Hermoso, A.,
1162 Bansal, M., Garcia-Gonzalez, I., Sanchez-Munoz, M.S., Perea, J.R., et al. (2017). Dual
1163 ifgMosaic: A Versatile Method for Multispectral and Combinatorial Mosaic Gene-Function
1164 Analysis. Cell *170*, 800-814 e818. 10.1016/j.cell.2017.07.031.
1165 Radtke, F., Wilson, A., Stark, G., Bauer, M., van Meerwijk, J., MacDonald, H.R., and Aguet, M. (1999).
1166 Deficient T Cell Fate Specification in Mice with an Induced Inactivation of Notch1. Immunity
1167 *10*, 547-558. 10.1016/s1074-7613(00)80054-0.
1168 Rashbrook, V.S., Brash, J.T., and Ruhrberg, C. (2022). Cre toxicity in mouse models of cardiovascular
1169 physiology and disease. Nature Cardiovascular Research *1*, 806-816. 10.1038/s44161-022-
1170 00125-6.
1171 Rodriguez, C.I., Buchholz, F., Galloway, J., Sequerra, R., Kasper, J., Ayala, R., Stewart, A.F., and
1172 Dymecki, S.M. (2000). High-efficiency deleter mice show that FLPe is an alternative to Cre-
1173 loxP. Nat Genet *25*, 139-140.
1174 Schmidt-Supprian, M., and Rajewsky, K. (2007). Vagaries of conditional gene targeting. Nat Immunol
1175 *8*, 665-668. 10.1038/ni0707-665.

1176 Sharma, P., Yan, F., Doronina, V.A., Escuin-Ordinas, H., Ryan, M.D., and Brown, J.D. (2012). 2A
1177 peptides provide distinct solutions to driving stop-carry on translational recoding. Nucleic
1178 Acids Res *40*, 3143-3151. 10.1093/nar/gkr1176.
1179 Siebel, C., and Lendahl, U. (2017). Notch Signaling in Development, Tissue Homeostasis, and Disease.
1180 Physiol Rev *97*, 1235-1294. 10.1152/physrev.00005.2017.
1181 Snippert, H.J., van der Flier, L.G., Sato, T., van Es, J.H., van den Born, M., Kroon-Veenboer, C., Barker,
1182 N., Klein, A.M., van Rheenen, J., Simons, B.D., and Clevers, H. (2010). Intestinal crypt
1183 homeostasis results from neutral competition between symmetrically dividing Lgr5 stem
1184 cells. Cell *143*, 134-144. 10.1016/j.cell.2010.09.016.
1185 Srinivas, S., Watanabe, T., Lin, C.S., William, C.M., Tanabe, Y., Jessell, T.M., and Costantini, F. (2001).
1186 Cre reporter strains produced by targeted insertion of EYFP and ECFP into the ROSA26 locus.
1187 BMC Dev Biol *1*, 4.
1188 Wang, Y., Nakayama, M., Pitulescu, M.E., Schmidt, T.S., Bochenek, M.L., Sakakibara, A., Adams, S.,
1189 Davy, A., Deutsch, U., Luthi, U., et al. (2010). Ephrin-B2 controls VEGF-induced angiogenesis
1190 and lymphangiogenesis. Nature *465*, 483-486. nature09002 [pii]

1191 10.1038/nature09002.
1192 Wei, Y., Wang, Y.G., Jia, Y., Li, L., Yoon, J., Zhang, S., Wang, Z., Zhang, Y., Zhu, M., Sharma, T., et al.
1193 (2021). Liver homeostasis is maintained by midlobular zone 2 hepatocytes. Science *371*.
1194 10.1126/science.abb1625.
1195 Wilhelm, K., Happel, K., Eelen, G., Schoors, S., Oellerich, M.F., Lim, R., Zimmermann, B., Aspalter,
1196 I.M., Franco, C.A., Boettger, T., et al. (2016). FOXO1 couples metabolic activity and growth
1197 state in the vascular endothelium. Nature *529*, 216-220. 10.1038/nature16498.
1198 Zong, H. (2014). Generation and applications of MADM-based mouse genetic mosaic system.
1199 Methods Mol Biol *1194*, 187-201. 10.1007/978-1-4939-1215-5_10.
1200 Zong, H., Espinosa, J.S., Su, H.H., Muzumdar, M.D., and Luo, L. (2005). Mosaic analysis with double
1201 markers in mice. Cell *121*, 479-492. 10.1016/j.cell.2005.02.012.

1202

1203

1204

1205

Figure 1

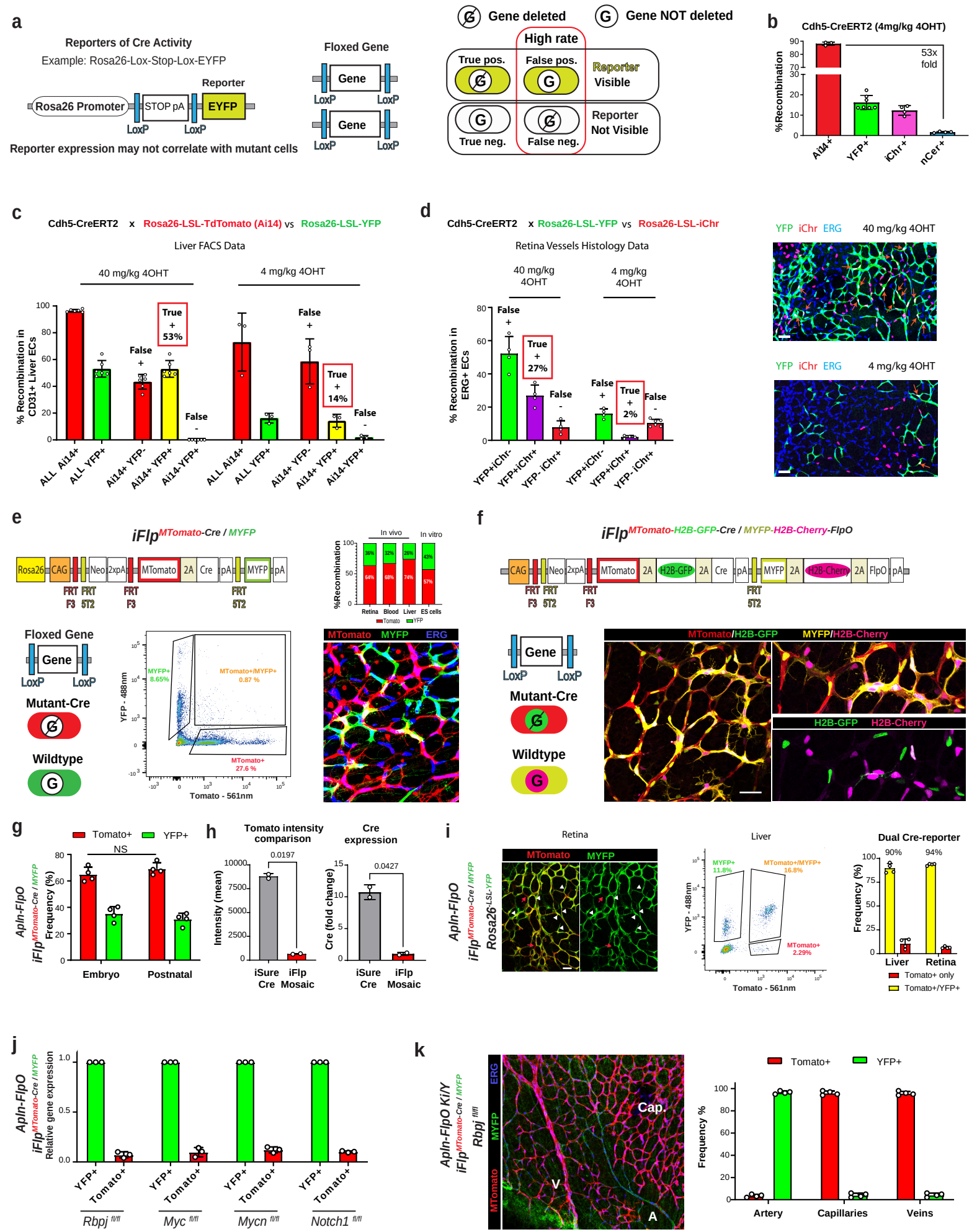
a
Reporters of Cre Activity
Example: Rosa26-Lox-Stop-Lox-EYFP
Reporter
Rosa26 Promoter
STOP pA
EYFP
LoxP
LoxP
Reporter expression may not correlate with mutant cells
Floxed Gene
Gene
Gene deleted
Gene NOT deleted
High rate
True pos.
False pos.
Reporter Visible
True neg.
False neg.
Reporter Not Visible
b
Cdh5-CreERT2 (4mg/kg 4OHT)
%Recombination
53x fold
Ai14+
YFP+
iChr+
nCer+
c
Cdh5-CreERT2 x Rosa26-LSL-TdTomato (Ai14) vs Rosa26-LSL-YFP
Liver FACS Data
40 mg/kg 4OHT
4 mg/kg 4OHT
% Recombination in CD31+ Liver ECs
True + 53%
False +
False -
True + 14%
ALL Ai14+
ALL YFP+
Ai14+ YFP-
Ai14+ YFP+
Ai14-YFP+
d
Cdh5-CreERT2 x Rosa26-LSL-YFP vs Rosa26-LSL-iChr
Retina Vessels Histology Data
% Recombination in ERG+ ECs
True + 27%
True + 2%
YFP+iChr-
YFP+iChr+
YFP- iChr+
YFP iChr ERG
40 mg/kg 4OHT
4 mg/kg 4OHT
e
iFlpMTomato-Cre / MYFP
Rosa26
CAG
Neo
2xpA
MTomato
2A
Cre
pA
MYFP
FRT F3
FRT 5T2
In vivo
In vitro
%Recombination
Retina
Blood
Liver
ES cells
Tomato
YFP
Floxed Gene
Gene
Mutant-Cre
Wildtype
MYFP+ 8.65%
MTomato+/MYFP+ 0.87 %
MTomato+ 27.6 %
YFP - 488nm
Tomato - 561nm
MTomato MYFP ERG
f
iFlpMTomato-H2B-GFP-Cre / MYFP-H2B-Cherry-FlpO
H2B-GFP
H2B-Cherry
FlpO
MTomato/H2B-GFP
MYFP/H2B-Cherry
g
Tomato+
YFP+
NS
Apln-FlpO
iFlpMTomato-Cre / MYFP
Frequency (%)
Embryo
Postnatal
h
Tomato intensity comparison
Cre expression
0.0197
0.0427
Intensity (mean)
Cre (fold change)
iSure Cre
iFlp Mosaic
i
Retina
Liver
Dual Cre-reporter
Apln-FlpO
iFlpMTomato-Cre / MYFP
Rosa26LSL-YFP
MYFP+ 11.8%
MTomato+/MYFP+ 16.8%
MTomato+ 2.29%
90%
94%
Tomato+ only
Tomato+/YFP+
j
Apln-FlpO
iFlpMTomato-Cre / MYFP
Relative gene expression
Rbpj fl/fl
Myc fl/fl
Mycn fl/fl
Notch1 fl/fl
k
Apln-FlpO KI/Y
iFlpMTomato-Cre / MYFP
Rbpj fl/fl
ERG
MYFP
MTomato
Cap
V
A
Frequency %
Artery
Capillaries
Veins

Figure 2

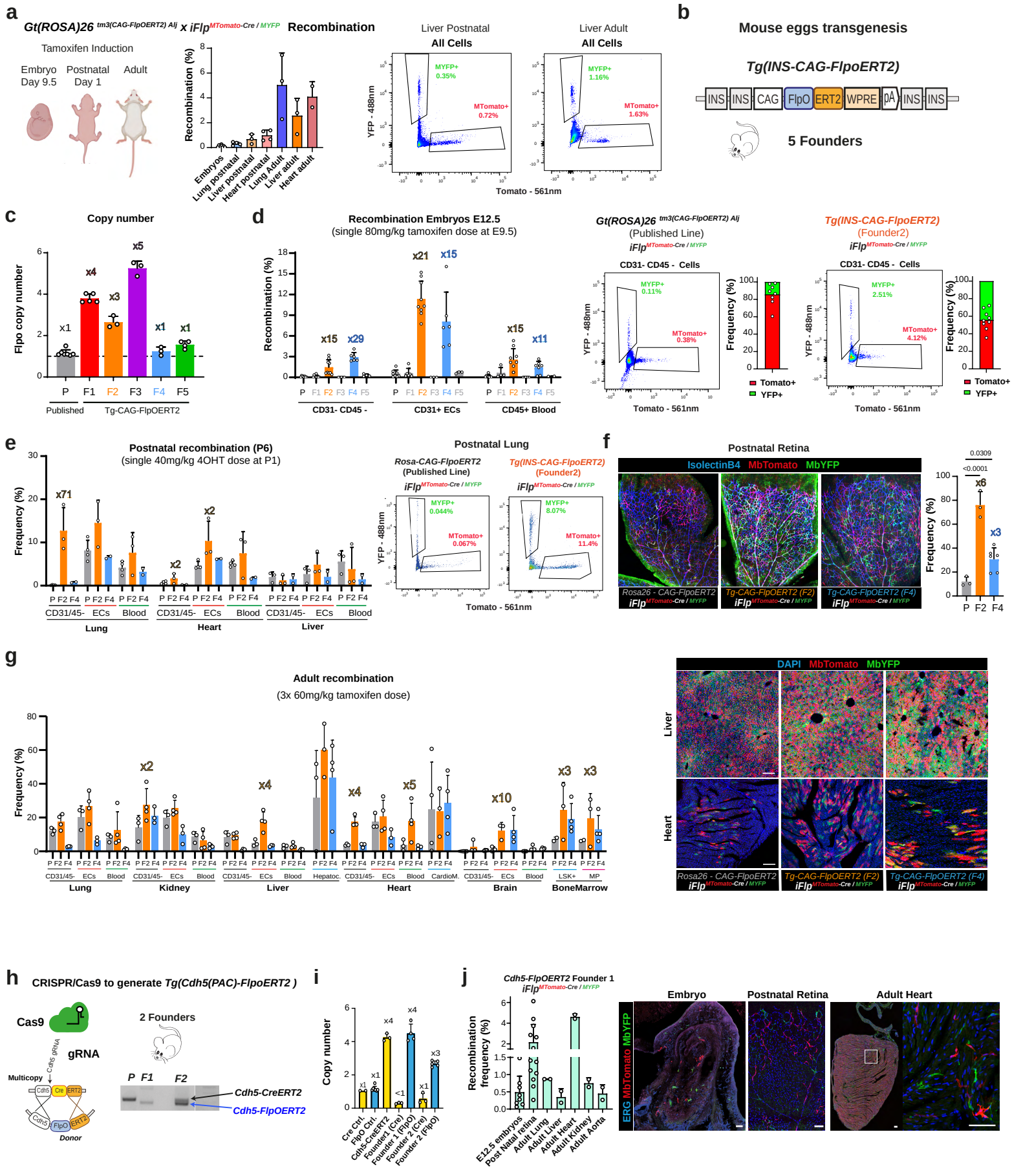
a
Gt(ROSA)26 tm3(CAG-FlpOERT2) Alj x iFlpMTomato-Cre / MYFP
Tamoxifen Induction
Embryo Day 9.5
Postnatal Day 1
Adult
Recombination
Recombination (%)
Embryos
Lung postnatal
Liver postnatal
Heart postnatal
Lung Adult
Liver adult
Heart adult
Liver Postnatal
All Cells
MYFP+ 0.35%
MTomato+ 0.72%
Liver Adult
All Cells
MYFP+ 1.16%
MTomato+ 1.63%
YFP - 488nm
Tomato - 561nm
b
Mouse eggs transgenesis
Tg(INS-CAG-FlpoERT2)
INS INS CAG FlpO ERT2 WPRE bA INS INS
5 Founders
c
Copy number
Flpo copy number
x1 x4 x3 x5 x1 x1
P F1 F2 F3 F4 F5
Published
Tg-CAG-FlpOERT2
d
Recombination Embryos E12.5
(single 80mg/kg tamoxifen dose at E9.5)
Recombination (%)
x15 x29 x21 x15 x15 x11
CD31- CD45 -
CD31+ ECs
CD45+ Blood
Gt(ROSA)26 tm3(CAG-FlpOERT2) Alj
(Published Line)
iFlpMTomato-Cre / MYFP
CD31- CD45 - Cells
MYFP+ 0.11%
MTomato+ 0.38%
Frequency (%)
Tomato+
YFP+
Tg(INS-CAG-FlpoERT2)
(Founder2)
iFlpMTomato-Cre / MYFP
CD31- CD45 - Cells
MYFP+ 2.51%
MTomato+ 4.12%
Tomato+
YFP+
e
Postnatal recombination (P6)
(single 40mg/kg 4OHT dose at P1)
Frequency (%)
x71 x2 x2
CD31/45- ECs Blood
Lung
Heart
Liver
Postnatal Lung
Rosa-CAG-FlpoERT2
(Published Line)
iFlpMTomato-Cre / MYFP
MYFP+ 0.044%
MTomato+ 0.067%
Tg(INS-CAG-FlpoERT2)
(Founder2)
iFlpMTomato-Cre / MYFP
MYFP+ 8.07%
MTomato+ 11.4%
f
Postnatal Retina
IsolectinB4 MbTomato MbYFP
Rosa26 - CAG-FlpoERT2
Tg-CAG-FlpOERT2 (F2)
Tg-CAG-FlpOERT2 (F4)
iFlpMTomato-Cre / MYFP
0.0309
<0.0001
x6 x3
P F2 F4
g
Adult recombination
(3x 60mg/kg tamoxifen dose)
Frequency (%)
x2 x4 x4 x5 x10 x3 x3
CD31/45- ECs Blood
Hepatoc.
CardioM.
LSK+ MP
Lung
Kidney
Liver
Heart
Brain
BoneMarrow
DAPI MbTomato MbYFP
Liver
Heart
Rosa26 - CAG-FlpoERT2
Tg-CAG-FlpOERT2 (F2)
Tg-CAG-FlpOERT2 (F4)
iFlpMTomato-Cre / MYFP
h
CRISPR/Cas9 to generate Tg(Cdh5(PAC)-FlpoERT2)
Cas9
gRNA
Cdh5 gRNA
Multicopy
Cdh5 Cre ERT2
Cdh5 FlpO ERT2
Donor
2 Founders
P F1 F2
Cdh5-CreERT2
Cdh5-FlpOERT2
i
Copy number
x1 x1 x4 <1 x4 x1 x3
Cre Ctrl.
FlpO Ctrl.
Cdh5-CreERT2
Founder1 (Cre)
Founder 1 (FlpO)
Founder 2 (Cre)
Founder 2 (FlpO)
j
Cdh5-FlpOERT2 Founder 1
iFlpMTomato-Cre / MYFP
Recombination frequency (%)
E12.5 embryos
Post Natal retina
Adult Lung
Adult Liver
Adult Heart
Adult Kidney
Adult Aorta
Embryo
Postnatal Retina
Adult Heart
ERG MbTomato MbYFP

Figure 3

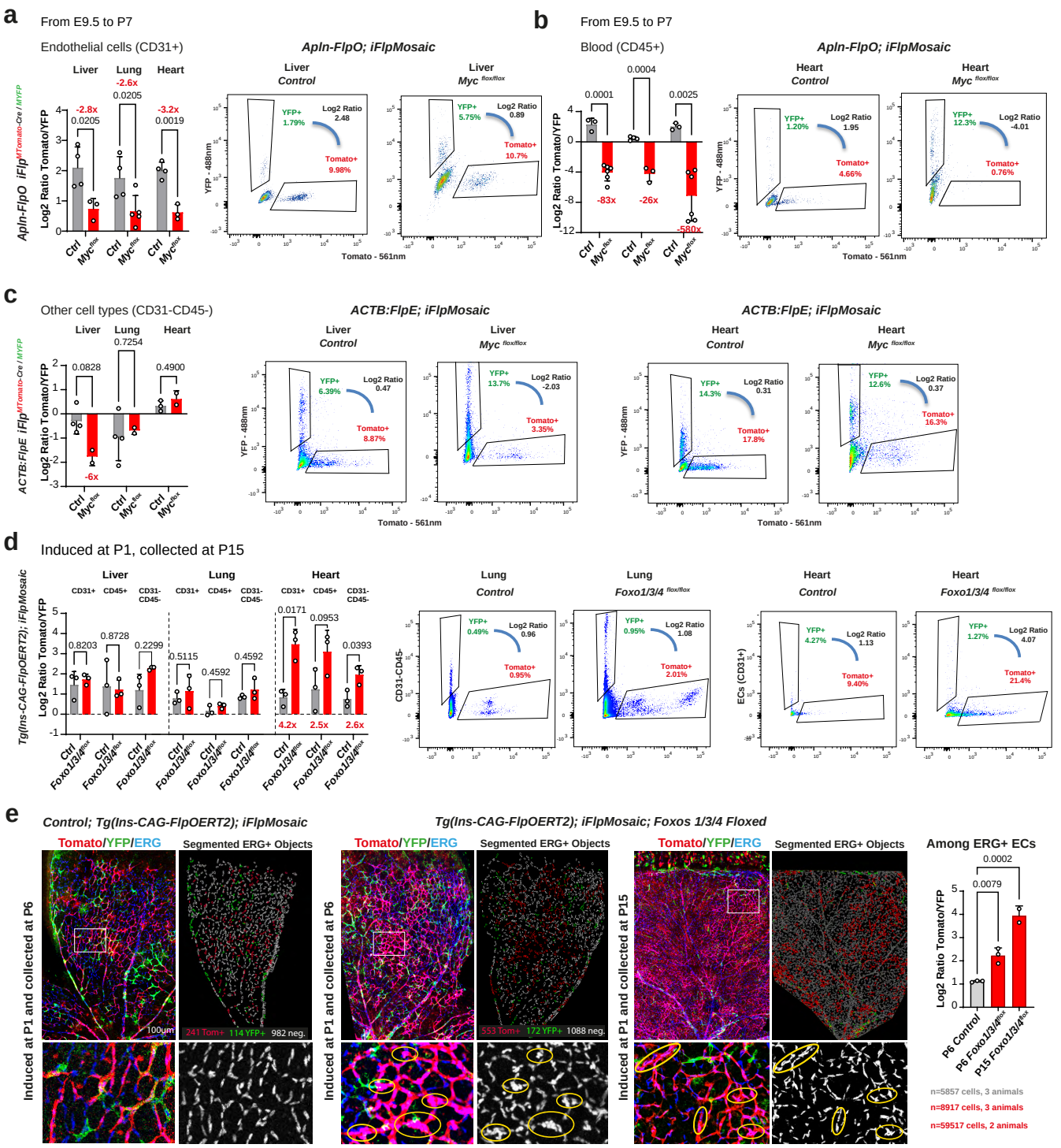
a
From E9.5 to P7
Endothelial cells (CD31+)
Apln-FlpO; iFlpMosaic
Liver
Lung
Heart
-2.8x
0.0205
-2.6x
0.0205
-3.2x
0.0019
Log2 Ratio Tomato/YFP
Apln-FlpO iFlp^MTomato-Cre / MYFP
Ctrl
Myc flox
Liver Control
Liver Myc flox/flox
YFP+ 1.79%
Log2 Ratio 2.48
Tomato+ 9.98%
YFP+ 5.75%
Log2 Ratio 0.89
Tomato+ 10.7%
YFP - 488nm
Tomato - 561nm
b
From E9.5 to P7
Blood (CD45+)
Apln-FlpO; iFlpMosaic
0.0001
0.0004
0.0025
-83x
-26x
-580x
Heart Control
Heart Myc flox/flox
YFP+ 1.20%
Log2 Ratio 1.95
Tomato+ 4.66%
YFP+ 12.3%
Log2 Ratio -4.01
Tomato+ 0.76%
c
Other cell types (CD31-CD45-)
ACTB:FlpE; iFlpMosaic
0.0828
0.7254
0.4900
-6x
ACTB:FlpE iFlp^MTomato-Cre / MYFP
YFP+ 6.39%
Log2 Ratio 0.47
Tomato+ 8.87%
YFP+ 13.7%
Log2 Ratio -2.03
Tomato+ 3.35%
YFP+ 14.3%
Log2 Ratio 0.31
Tomato+ 17.8%
YFP+ 12.6%
Log2 Ratio 0.37
Tomato+ 16.3%
d
Induced at P1, collected at P15
CD31+
CD45+
CD31-CD45-
0.8203
0.8728
0.2299
0.5115
0.4592
0.4592
0.0171
0.0953
0.0393
4.2x
2.5x
2.6x
Tg(Ins-CAG-FlpOERT2); iFlpMosaic
Ctrl
Foxo1/3/4 flox
Lung Control
Lung Foxo1/3/4 flox/flox
Heart Control
Heart Foxo1/3/4 flox/flox
CD31-CD45-
ECs (CD31+)
YFP+ 0.49%
Log2 Ratio 0.96
Tomato+ 0.95%
YFP+ 0.95%
Log2 Ratio 1.08
Tomato+ 2.01%
YFP+ 4.27%
Log2 Ratio 1.13
Tomato+ 9.40%
YFP+ 1.27%
Log2 Ratio 4.07
Tomato+ 21.4%
e
Control; Tg(Ins-CAG-FlpOERT2); iFlpMosaic
Tg(Ins-CAG-FlpOERT2); iFlpMosaic; Foxos 1/3/4 Floxed
Tomato/YFP/ERG
Segmented ERG+ Objects
Induced at P1 and collected at P6
Induced at P1 and collected at P15
100µm
241 Tom+ 114 YFP+ 982 neg.
553 Tom+ 172 YFP+ 1088 neg.
Among ERG+ ECs
0.0002
0.0079
Log2 Ratio Tomato/YFP
P6 Control
P6 Foxo1/3/4 flox
P15 Foxo1/3/4 flox
n=5857 cells, 3 animals
n=8917 cells, 3 animals
n=59517 cells, 2 animals

Figure 4

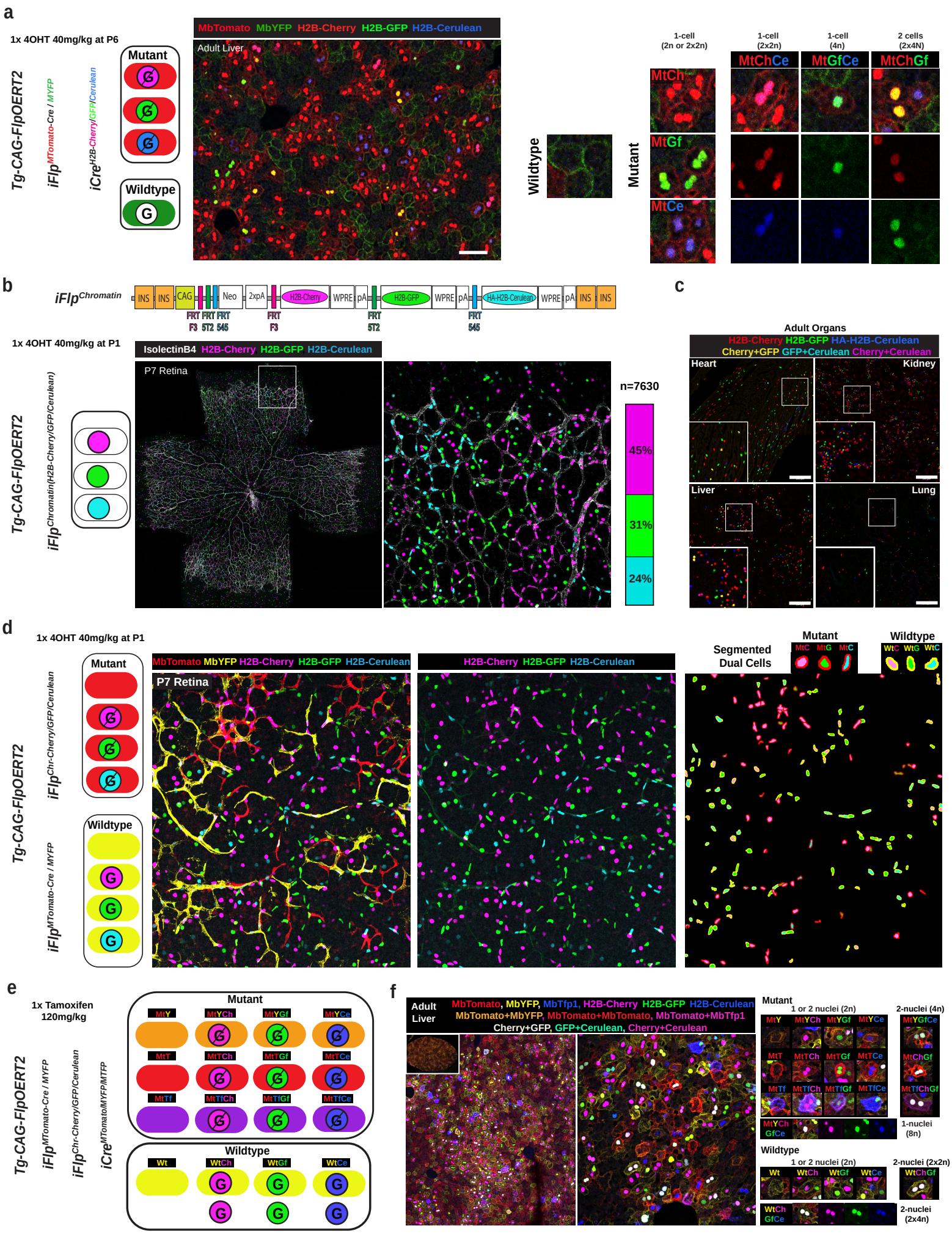
a
1x 4OHT 40mg/kg at P6
Tg-CAG-FlpOERT2
iFlp MTomato-Cre / MYFP
iCre H2B-Cherry/GFP/Cerulean
Mutant
Wildtype
MbTomato MbYFP H2B-Cherry H2B-GFP H2B-Cerulean
Adult Liver
Wildtype
Mutant
1-cell (2n or 2x2n)
1-cell (2x2n)
1-cell (4n)
2 cells (2x4N)
MtCh
MtGf
MtCe
MtChCe
MtGfCe
MtChGf
b
iFlp Chromatin
INS INS CAG Neo 2xpA H2B-Cherry WPRE pA H2B-GFP WPRE pA HA-H2B-Cerulean WPRE pA INS INS
FRT FRT FRT
F3 5T2 545
FRT
F3
FRT
5T2
FRT
545
1x 4OHT 40mg/kg at P1
Tg-CAG-FlpOERT2
iFlp Chromatin(H2B-Cherry/GFP/Cerulean)
IsolectinB4 H2B-Cherry H2B-GFP H2B-Cerulean
P7 Retina
n=7630
45%
31%
24%
c
Adult Organs
H2B-Cherry H2B-GFP HA-H2B-Cerulean
Cherry+GFP GFP+Cerulean Cherry+Cerulean
Heart
Kidney
Liver
Lung
d
1x 4OHT 40mg/kg at P1
Tg-CAG-FlpOERT2
iFlp Chr-Cherry/GFP/Cerulean
iFlp MTomato-Cre / MYFP
Mutant
Wildtype
MbTomato MbYFP H2B-Cherry H2B-GFP H2B-Cerulean
P7 Retina
H2B-Cherry H2B-GFP H2B-Cerulean
Segmented Dual Cells
Mutant
Wildtype
MtC MtG MtC
WtC WtG WtC
e
1x Tamoxifen 120mg/kg
Tg-CAG-FlpOERT2
iFlp MTomato-Cre / MYFP
iFlp Chr-Cherry/GFP/Cerulean
iCre MTomato/MYFP/MTFP
Mutant
MtY MtYCh MtYGf MtYCe
MtT MtTCh MtTGf MtTCe
MtTf MtTfCh MtTfGf MtTfCe
Wildtype
Wt WtCh WtGf WtCe
f
Adult Liver
MbTomato, MbYFP, MbTfp1, H2B-Cherry H2B-GFP H2B-Cerulean
MbTomato+MbYFP, MbTomato+MbTomato, MbTomato+MbTfp1
Cherry+GFP, GFP+Cerulean, Cherry+Cerulean
Mutant
1 or 2 nuclei (2n)
2-nuclei (4n)
1-nuclei (8n)
Wildtype
1 or 2 nuclei (2n)
2-nuclei (2x2n)
2-nuclei (2x4n)

Figure 5

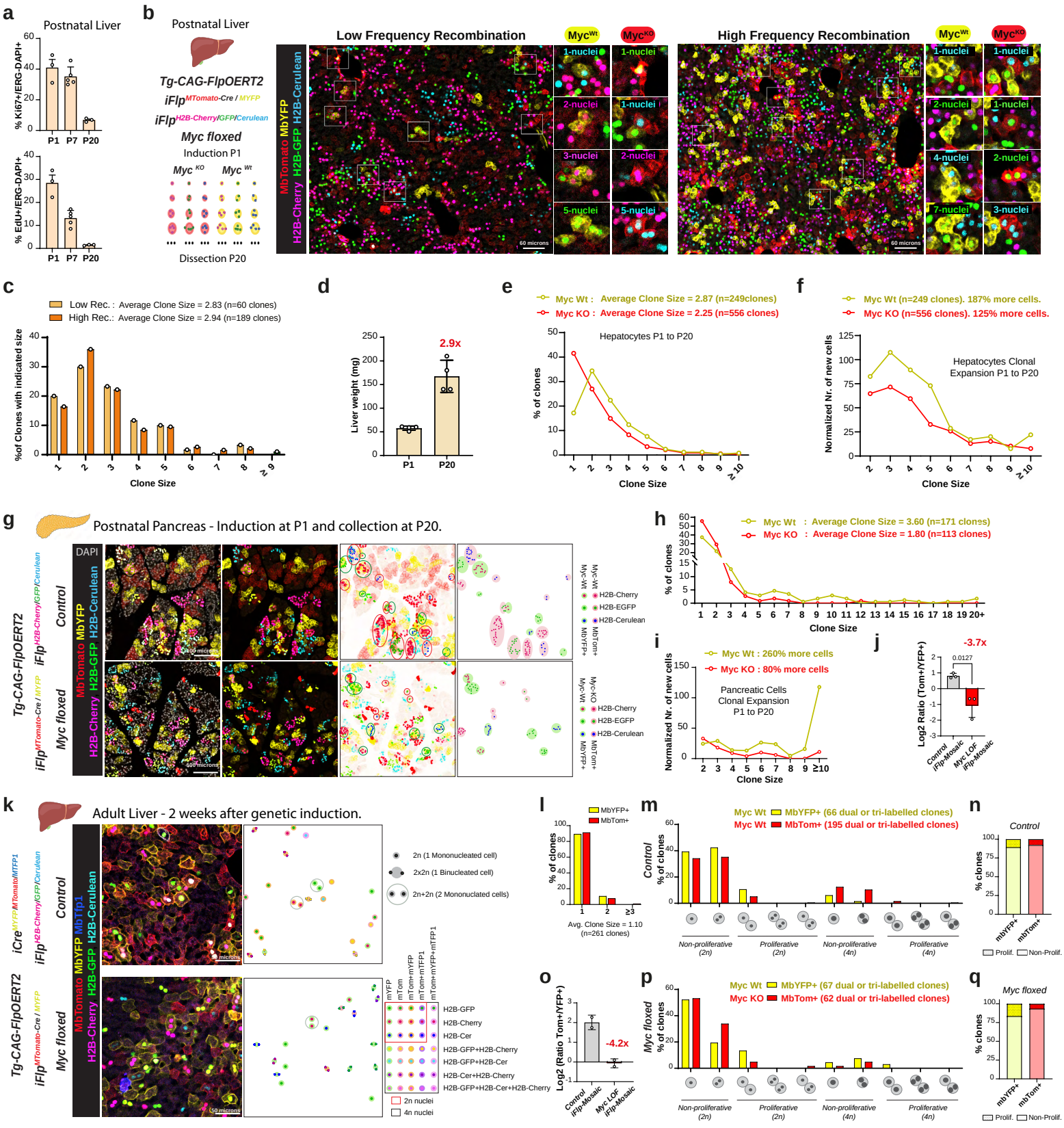
a
Postnatal Liver
% Ki67+/ERG-DAPI+
% EdU+/ERG-DAPI+
P1 P7 P20
b
Postnatal Liver
Tg-CAG-FlpOERT2
iFlp MTomato-Cre / MYFP
iFlp H2B-Cherry/GFP/Cerulean
Myc floxed
Induction P1
Myc KO Myc Wt
Dissection P20
Low Frequency Recombination
High Frequency Recombination
MbTomato MbYFP
H2B-Cherry H2B-GFP H2B-Cerulean
1-nuclei
2-nuclei
3-nuclei
4-nuclei
5-nuclei
7-nuclei
60 microns
c
Low Rec. : Average Clone Size = 2.83 (n=60 clones)
High Rec.: Average Clone Size = 2.94 (n=189 clones)
%of Clones with indicated size
Clone Size
d
2.9x
Liver weight (mg)
P1 P20
e
Myc Wt : Average Clone Size = 2.87 (n=249clones)
Myc KO : Average Clone Size = 2.25 (n=556 clones)
Hepatocytes P1 to P20
% of clones
Clone Size
f
Myc Wt (n=249 clones). 187% more cells.
Myc KO (n=556 clones). 125% more cells.
Hepatocytes Clonal Expansion P1 to P20
Normalized Nr. of new cells
Clone Size
g
Postnatal Pancreas - Induction at P1 and collection at P20.
Tg-CAG-FlpOERT2
iFlp MTomato-Cre / MYFP
iFlp H2B-Cherry/GFP/Cerulean
Control
Myc floxed
DAPI
MbTomato MbYFP
H2B-Cherry H2B-GFP H2B-Cerulean
400 microns
Myc-Wt
Myc-KO
MbYFP+
MbTom+
H2B-Cherry
H2B-EGFP
H2B-Cerulean
h
Myc Wt : Average Clone Size = 3.60 (n=171 clones)
Myc KO : Average Clone Size = 1.80 (n=113 clones)
% of clones
Clone Size
i
Myc Wt : 260% more cells
Myc KO : 80% more cells
Pancreatic Cells Clonal Expansion P1 to P20
Normalized Nr. of new cells
Clone Size
j
-3.7x
0.0127
Log2 Ratio (Tom+/YFP+)
Control iFlp-Mosaic
Myc LOF iFlp-Mosaic
k
Adult Liver - 2 weeks after genetic induction.
iCre MYFP-MTomato/MTFP1
iFlp H2B-Cherry/GFP/Cerulean
Control
Tg-CAG-FlpOERT2
iFlp MTomato-Cre / MYFP
Myc floxed
MbTomato MbYFP MbTfp1
H2B-Cherry H2B-GFP H2B-Cerulean
50 microns
2n (1 Mononucleated cell)
2x2n (1 Binucleated cell)
2n+2n (2 Mononuclated cells)
mYFP
mTom
mTom+mYFP
mTom+mTFP1
mTom+mYFP+mTFP1
H2B-GFP
H2B-Cherry
H2B-Cer
H2B-GFP+H2B-Cherry
H2B-GFP+H2B-Cer
H2B-Cer+H2B-Cherry
H2B-GFP+H2B-Cer+H2B-Cherry
2n nuclei
4n nuclei
l
MbYFP+
MbTom+
% of clones
Avg. Clone Size = 1.10 (n=261 clones)
m
Myc Wt MbYFP+ (66 dual or tri-labelled clones)
Myc Wt MbTom+ (195 dual or tri-labelled clones)
Control
% of clones
Non-proliferative (2n)
Proliferative (2n)
Non-proliferative (4n)
Proliferative (4n)
n
Control
% clones
mbYFP+
mbTom+
Prolif.
Non-Prolif.
o
-4.2x
Log2 (Ratio Tom+/YFP+)
Control iFlp-Mosaic
Myc LOF iFlp-Mosaic
p
Myc Wt MbYFP+ (67 dual or tri-labelled clones)
Myc KO MbTom+ (62 dual or tri-labelled clones)
Myc floxed
% of clones
Non-proliferative (2n)
Proliferative (2n)
Non-proliferative (4n)
Proliferative (4n)
q
Myc floxed
% clones
mbYFP+
mbTom+
Prolif.
Non-Prolif.

Figure 6

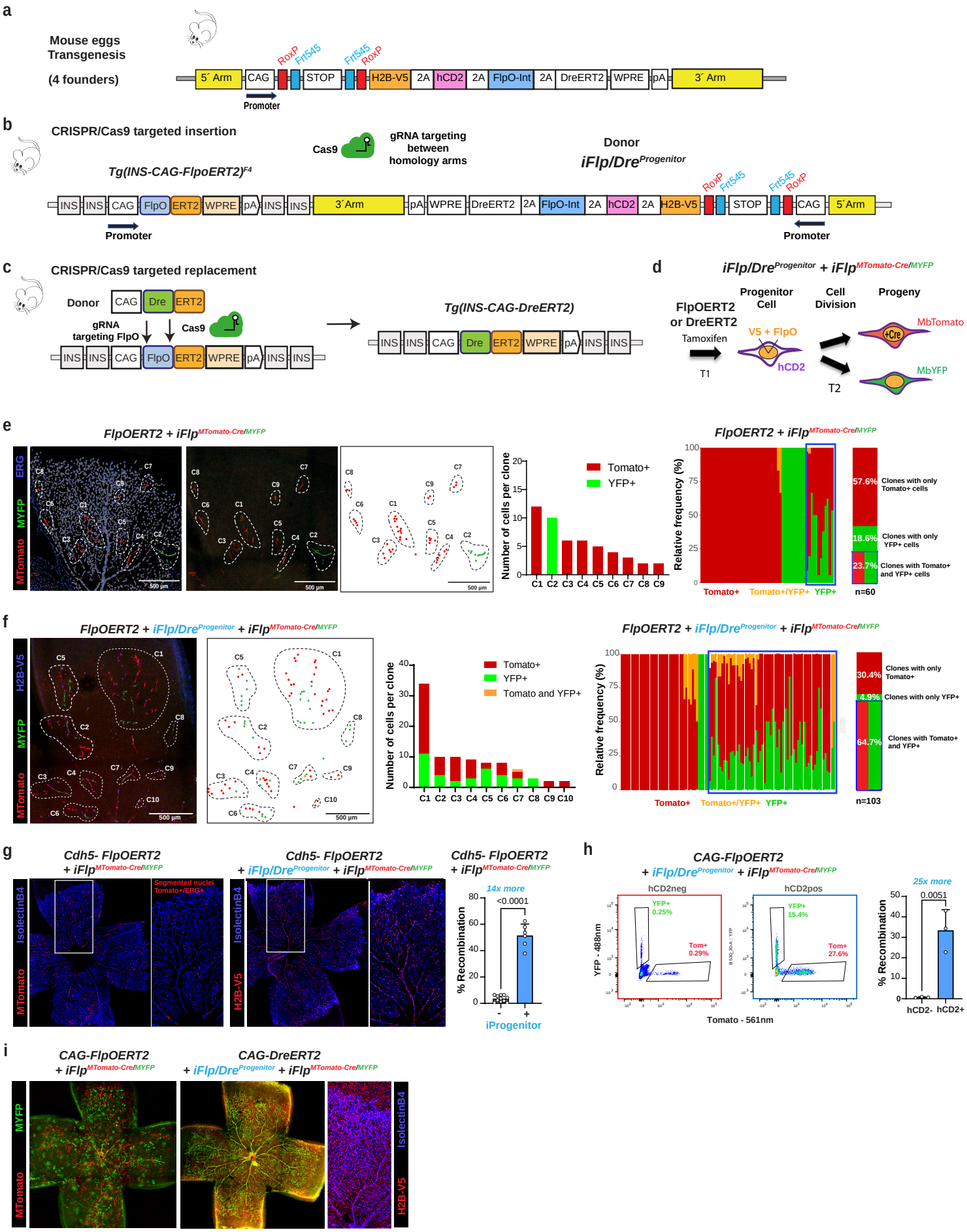
a
Mouse eggs
Transgenesis
(4 founders)
5´ Arm
CAG
RoxP
Frt545
STOP
Frt545
RoxP
H2B-V5
2A
hCD2
2A
FlpO-Int
2A
DreERT2
WPRE
pA
3´ Arm
Promoter
b
CRISPR/Cas9 targeted insertion
Cas9
gRNA targeting between homology arms
Donor
iFlp/Dre Progenitor
Tg(INS-CAG-FlpoERT2)F4
INS
CAG
FlpO
ERT2
WPRE
pA
3´Arm
5´Arm
Promoter
c
CRISPR/Cas9 targeted replacement
Donor
Dre
gRNA targeting FlpO
Tg(INS-CAG-DreERT2)
d
iFlp/Dre Progenitor + iFlp MTomato-Cre/MYFP
FlpOERT2 or DreERT2
Tamoxifen
T1
Progenitor Cell
V5 + FlpO
hCD2
Cell Division
T2
Progeny
MbTomato
+Cre
MbYFP
e
FlpOERT2 + iFlp MTomato-Cre/MYFP
ERG
MYFP
MTomato
500 µm
Number of cells per clone
Tomato+
YFP+
Relative frequency (%)
Tomato+
Tomato+/YFP+
YFP+
57.6% Clones with only Tomato+ cells
18.6% Clones with only YFP+ cells
23.7% Clones with Tomato+ and YFP+ cells
n=60
f
FlpOERT2 + iFlp/Dre Progenitor + iFlp MTomato-Cre/MYFP
H2B-V5
Tomato and YFP+
30.4% Clones with only Tomato+
4.9% Clones with only YFP+
64.7% Clones with Tomato+ and YFP+
n=103
g
Cdh5- FlpOERT2 + iFlp MTomato-Cre/MYFP
Cdh5- FlpOERT2 + iFlp/Dre Progenitor + iFlp MTomato-Cre/MYFP
IsolectinB4
Segmented nuclei Tomato+/ERG+
14x more
<0.0001
% Recombination
iProgenitor
h
CAG-FlpOERT2 + iFlp/Dre Progenitor + iFlp MTomato-Cre/MYFP
hCD2neg
hCD2pos
YFP+ 0.25%
Tom+ 0.29%
YFP+ 15.4%
Tom+ 27.6%
YFP - 488nm
Tomato - 561nm
25x more
0.0051
hCD2-
hCD2+
i
CAG-FlpOERT2 + iFlp MTomato-Cre/MYFP
CAG-DreERT2 + iFlp/Dre Progenitor + iFlp MTomato-Cre/MYFP

Figure 7

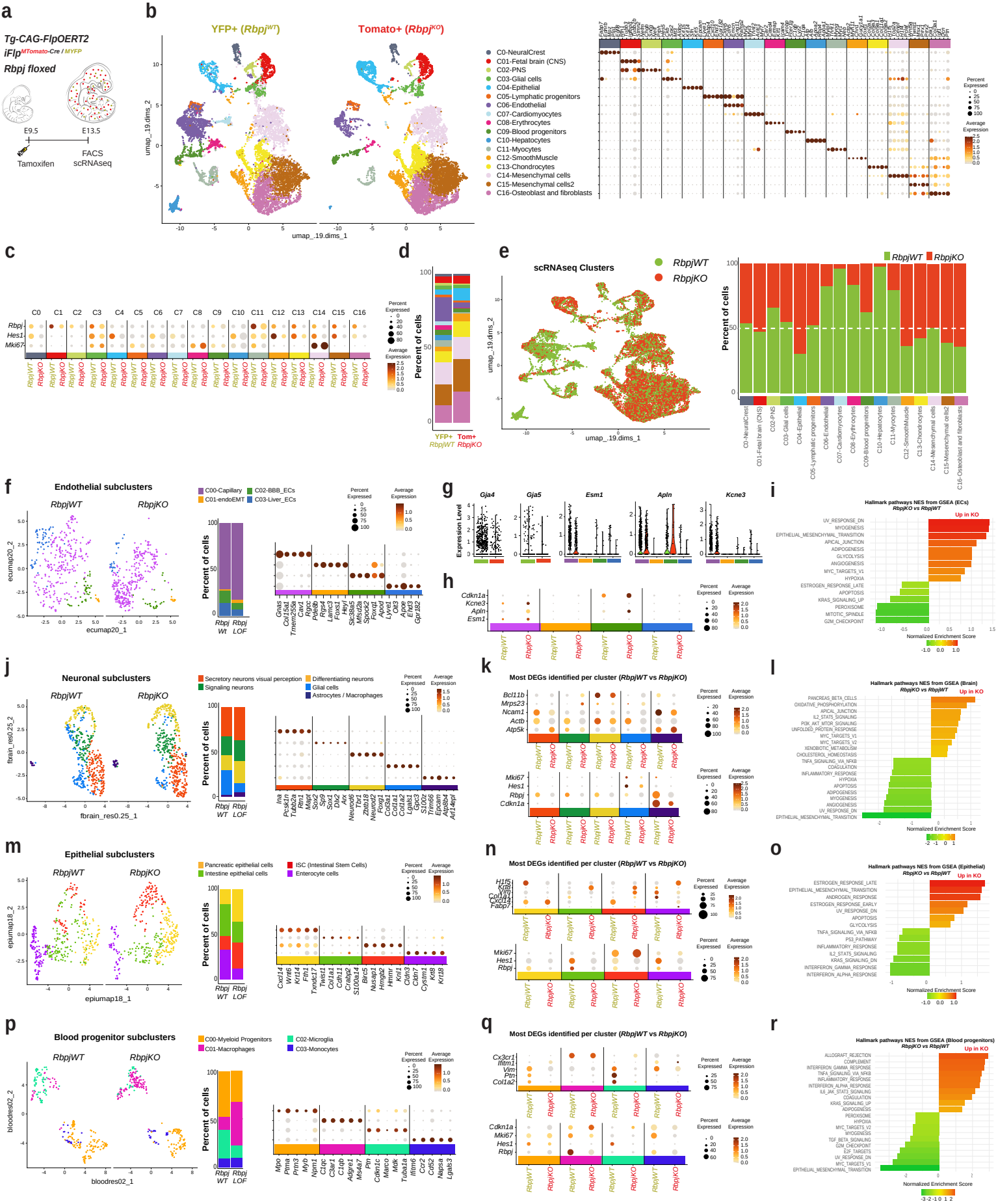
a
Tg-CAG-FlpOERT2
iFlp MTomato-Cre / MYFP
Rbpj floxed
E9.5
E13.5
Tamoxifen
FACS
scRNAseq
b
YFP+ (RbpjWT)
Tomato+ (RbpjKO)
umap_.19.dims_2
umap_.19.dims_1
C0-NeuralCrest
C01-Fetal brain (CNS)
C02-PNS
C03-Glial cells
C04-Epithelial
C05-Lymphatic progenitors
C06-Endothelial
C07-Cardiomyocytes
C08-Erythrocytes
C09-Blood progenitors
C10-Hepatocytes
C11-Myocytes
C12-SmoothMuscle
C13-Chondrocytes
C14-Mesenchymal cells
C15-Mesenchymal cells2
C16-Osteoblast and fibroblasts
Percent Expressed
Average Expression
c
Rbpj
Hes1
Mki67
d
Percent of cells
YFP+ RbpjWT
Tom+ RbpjKO
e
scRNAseq Clusters
RbpjWT
RbpjKO
umap_.19.dims_2
umap_.19.dims_1
Percent of cells
f
Endothelial subclusters
RbpjWT
RbpjKO
ecumap20_2
ecumap20_1
C00-Capillary
C01-endoEMT
C02-BBB_ECs
C03-Liver_ECs
Percent of cells
Rbpj Wt
Rbpj LOF
g
Gja4
Gja5
Esm1
Apln
Kcne3
Expression Level
h
Cdkn1a
Kcne3
Apln
Esm1
i
Hallmark pathways NES from GSEA (ECs)
RbpjKO vs RbpjWT
Up in KO
UV_RESPONSE_DN
MYOGENESIS
EPITHELIAL_MESENCHYMAL_TRANSITION
APICAL_JUNCTION
ADIPOGENESIS
GLYCOLYSIS
ANGIOGENESIS
MYC_TARGETS_V1
HYPOXIA
ESTROGEN_RESPONSE_LATE
APOPTOSIS
KRAS_SIGNALING_UP
PEROXISOME
MITOTIC_SPINDLE
G2M_CHECKPOINT
Normalized Enrichment Score
j
Neuronal subclusters
RbpjWT
RbpjKO
fbrain_res0.25_2
fbrain_res0.25_1
Secretory neurons visual perception
Signaling neurons
Differentiating neurons
Glial cells
Astrocytes / Macrophages
Percent of cells
Rbpj WT
Rbpj LOF
k
Most DEGs identified per cluster (RbpjWT vs RbpjKO)
Bcl11b
Mrps23
Ncam1
Actb
Atp5k
Mki67
Hes1
Rbpj
Cdkn1a
l
Hallmark pathways NES from GSEA (Brain)
RbpjKO vs RbpjWT
Up in KO
PANCREAS_BETA_CELLS
OXIDATIVE_PHOSPHORYLATION
APICAL_JUNCTION
IL2_STAT5_SIGNALING
PI3K_AKT_MTOR_SIGNALING
UNFOLDED_PROTEIN_RESPONSE
MYC_TARGETS_V1
MYC_TARGETS_V2
XENOBIOTIC_METABOLISM
CHOLESTEROL_HOMEOSTASIS
TNFA_SIGNALING_VIA_NFKB
COAGULATION
INFLAMMATORY_RESPONSE
HYPOXIA
APOPTOSIS
ADIPOGENESIS
MYOGENESIS
ANGIOGENESIS
UV_RESPONSE_DN
EPITHELIAL_MESENCHYMAL_TRANSITION
Normalized Enrichment Score
m
Epithelial subclusters
RbpjWT
RbpjKO
epiumap18_2
epiumap18_1
Pancreatic epithelial cells
Intestine epithelial cells
ISC (Intestinal Stem Cells)
Enterocyte cells
Percent of cells
Rbpj WT
Rbpj LOF
n
Most DEGs identified per cluster (RbpjWT vs RbpjKO)
Mki67
Hes1
Rbpj
o
Hallmark pathways NES from GSEA (Epithelial)
RbpjKO vs RbpjWT
Up in KO
ESTROGEN_RESPONSE_LATE
EPITHELIAL_MESENCHYMAL_TRANSITION
ANDROGEN_RESPONSE
ESTROGEN_RESPONSE_EARLY
UV_RESPONSE_DN
APOPTOSIS
GLYCOLYSIS
TNFA_SIGNALING_VIA_NFKB
P53_PATHWAY
INFLAMMATORY_RESPONSE
IL2_STAT5_SIGNALING
KRAS_SIGNALING_DN
INTERFERON_GAMMA_RESPONSE
INTERFERON_ALPHA_RESPONSE
Normalized Enrichment Score
p
Blood progenitor subclusters
RbpjWT
RbpjKO
bloodres02_2
bloodres02_1
C00-Myeloid Progenitors
C01-Macrophages
C02-Microglia
C03-Monocytes
Percent of cells
Rbpj WT
Rbpj LOF
q
Most DEGs identified per cluster (RbpjWT vs RbpjKO)
Cx3cr1
Ifitm1
Vim
Ptn
Col1a2
Cdkn1a
Mki67
Hes1
Rbpj
r
Hallmark pathways NES from GSEA (Blood progenitors)
RbpjKO vs RbpjWT
Up in KO
ALLOGRAFT_REJECTION
COMPLEMENT
INTERFERON_GAMMA_RESPONSE
TNFA_SIGNALING_VIA_NFKB
INFLAMMATORY_RESPONSE
INTERFERON_ALPHA_RESPONSE
IL6_JAK_STAT3_SIGNALING
COAGULATION
KRAS_SIGNALING_UP
ADIPOGENESIS
PEROXISOME
HYPOXIA
MYC_TARGETS_V2
MYOGENESIS
TGF_BETA_SIGNALING
G2M_CHECKPOINT
E2F_TARGETS
UV_RESPONSE_DN
MYC_TARGETS_V1
EPITHELIAL_MESENCHYMAL_TRANSITION
Normalized Enrichment Score

Supplementary Fig. 1

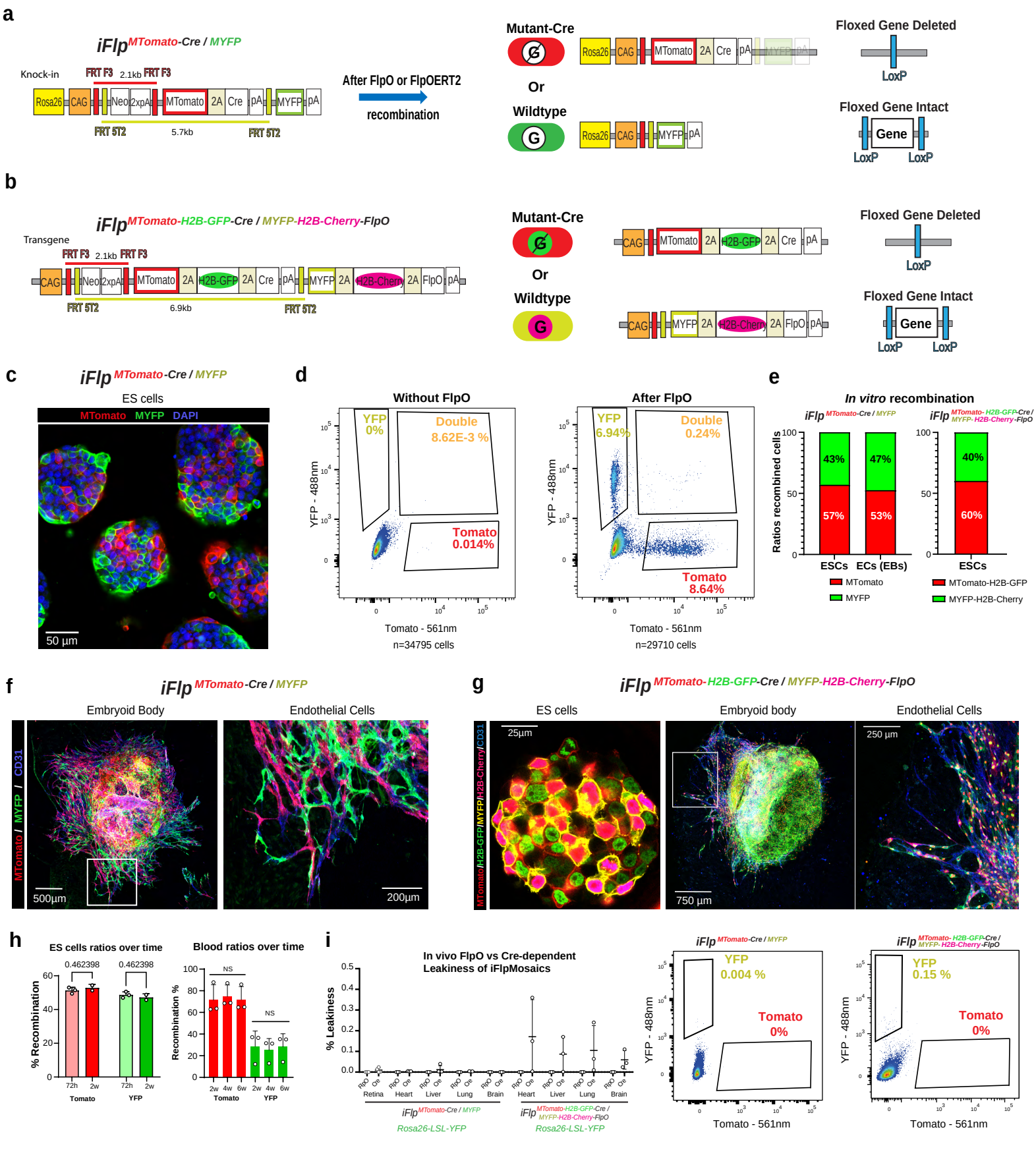

Supplementary Fig. 2

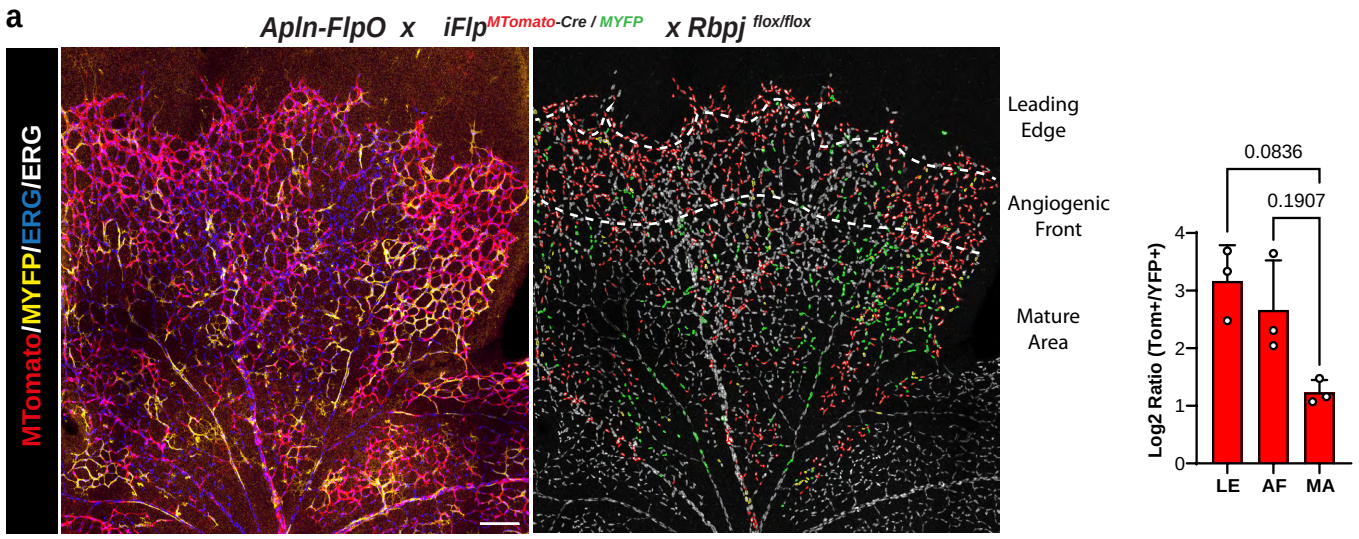

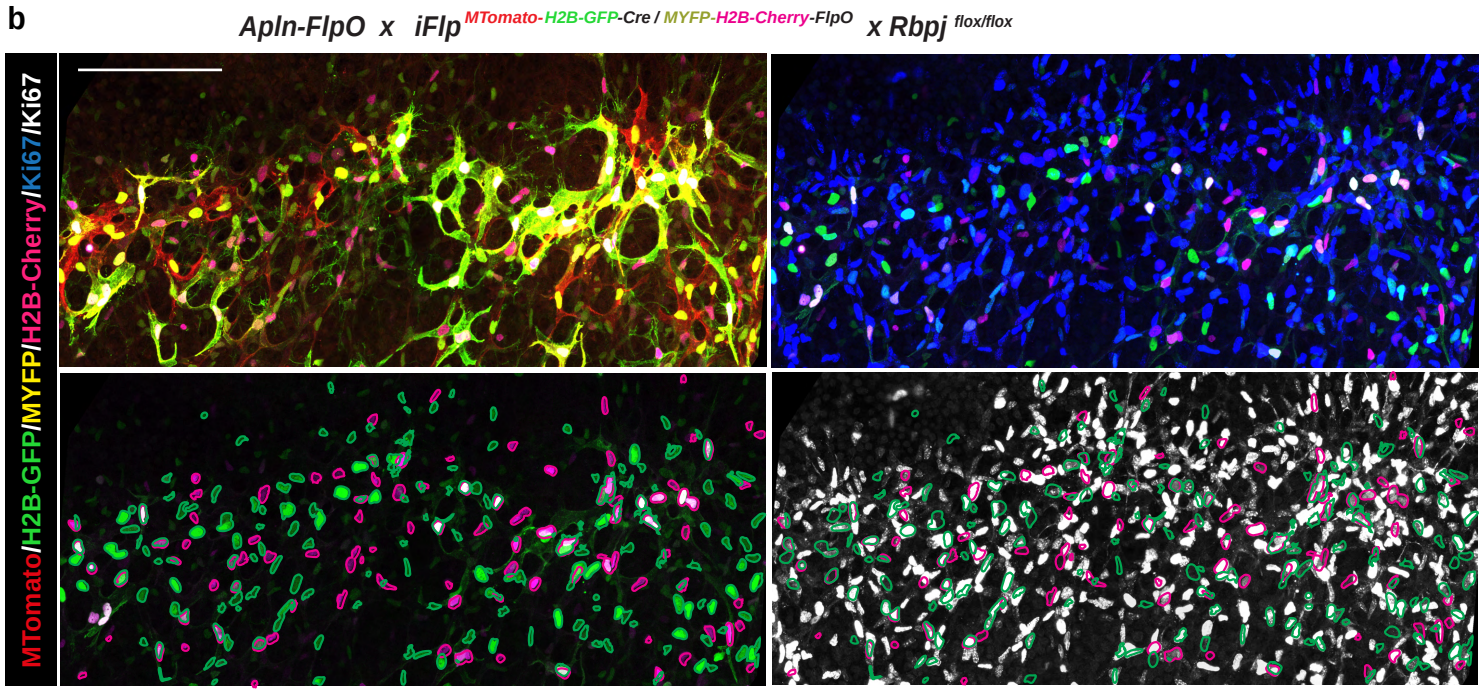

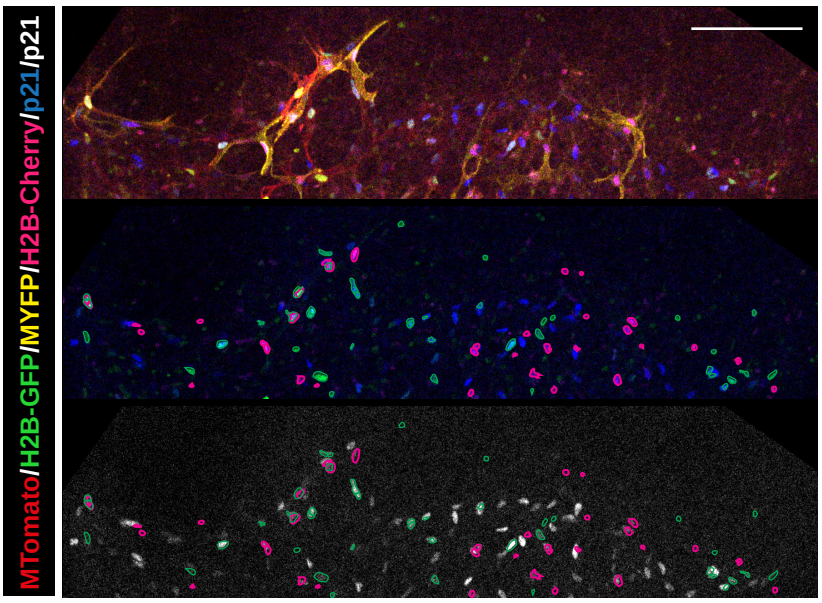

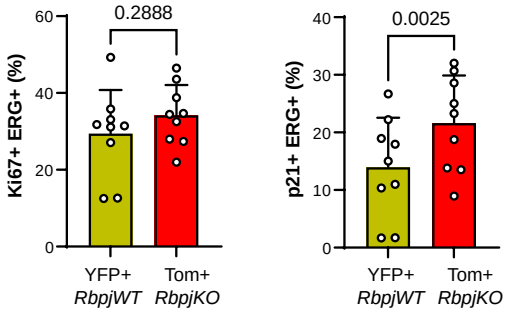

Supplementary Fig. 3

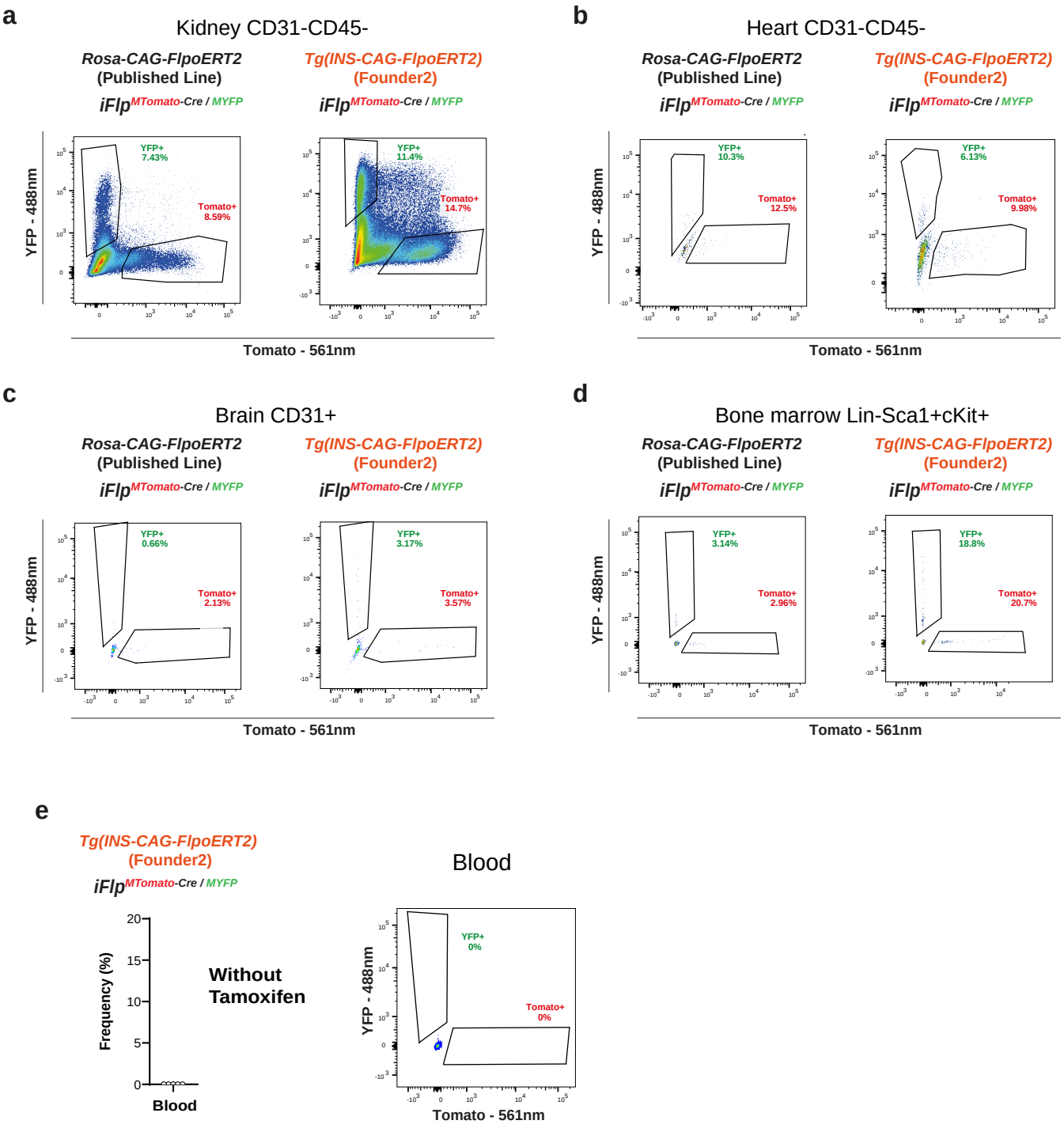

Supplementary Fig. 4

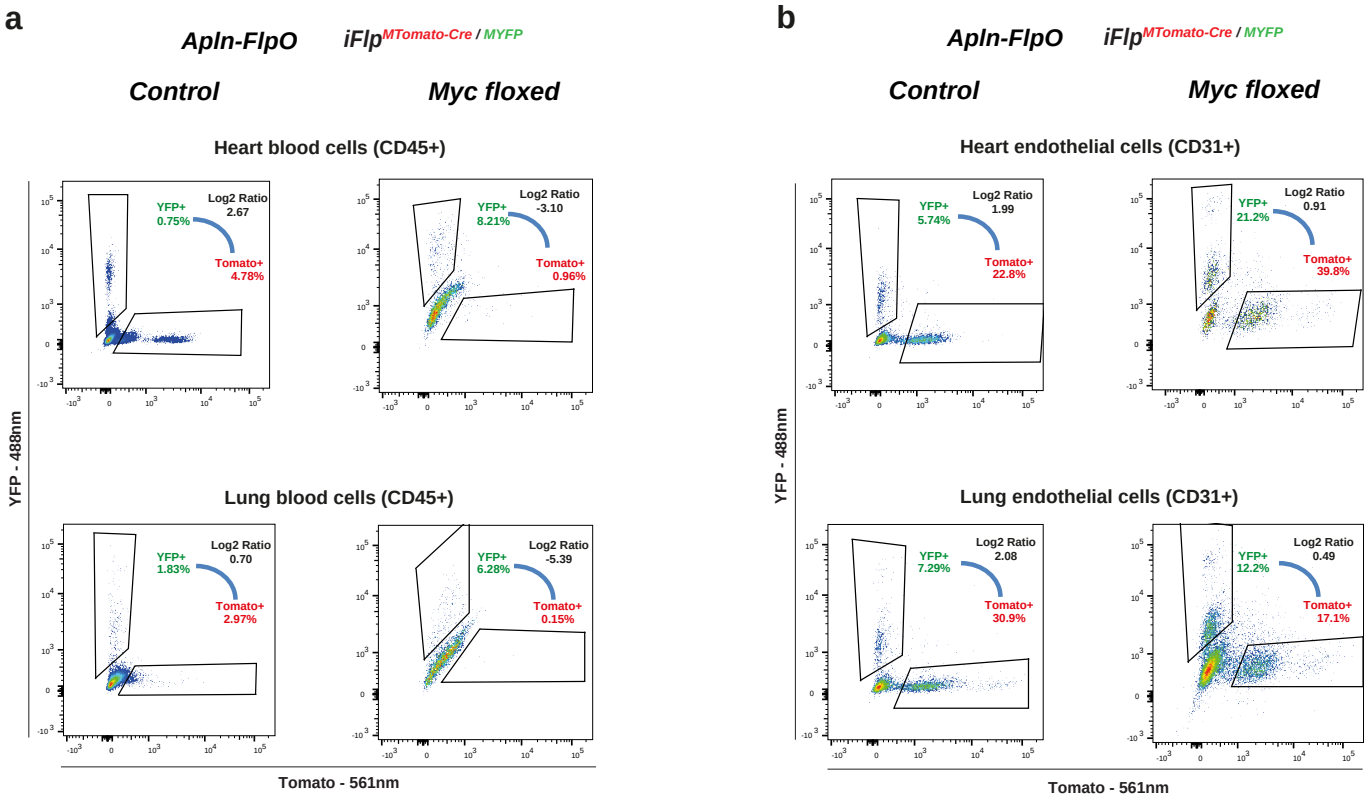

c

iChr2-Mosaic or iCreH2B-Cherry/GFP/Cerulean

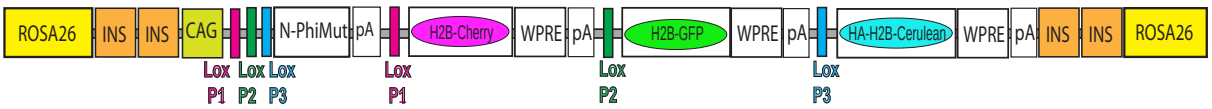

Supplementary Fig. 5

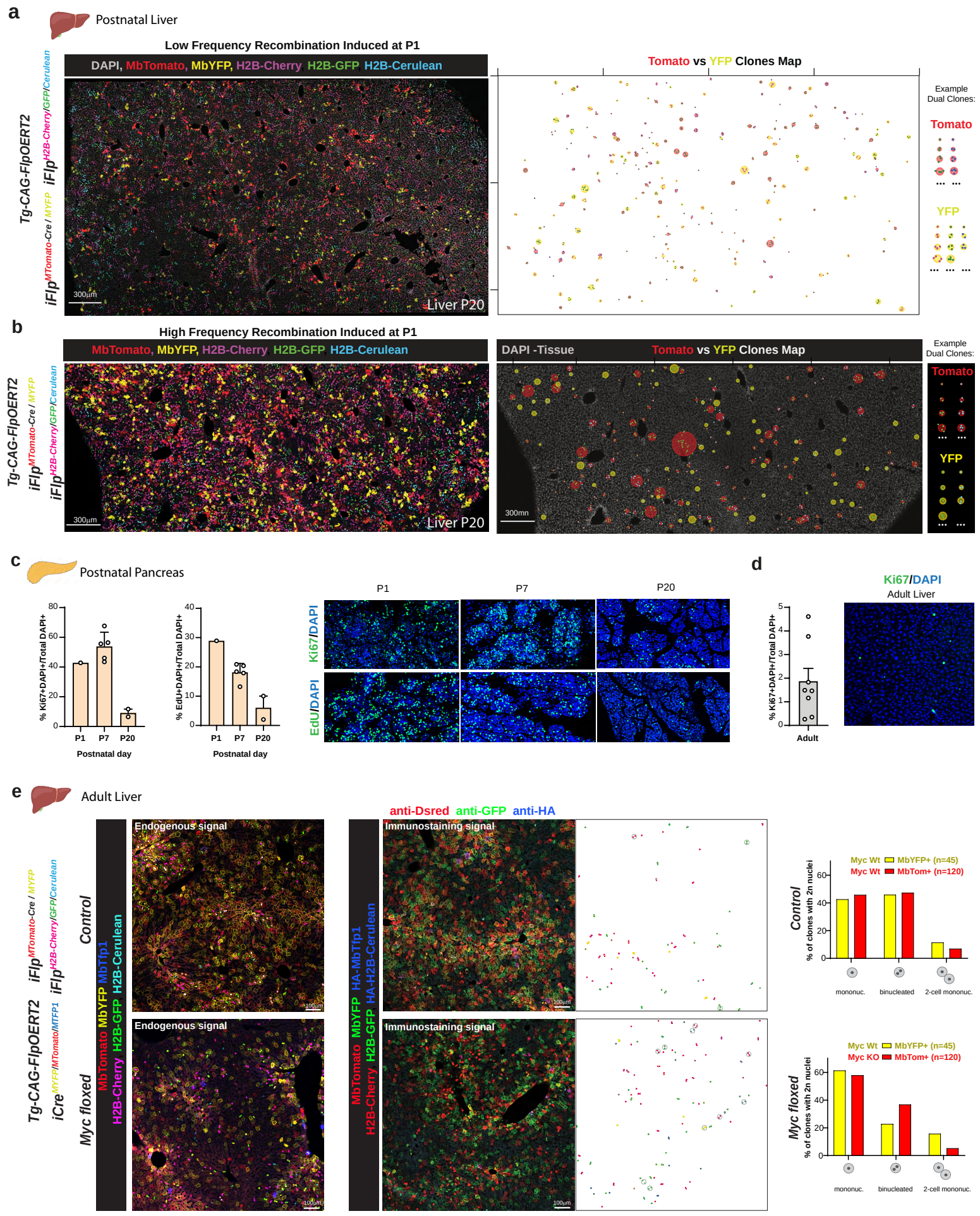

Supplementary Figure 6

a

FlpOERT2 + iFlp/Dre^{Progenitor} + iFlp$^{MTomato\text{-}Cre/MYFP}$

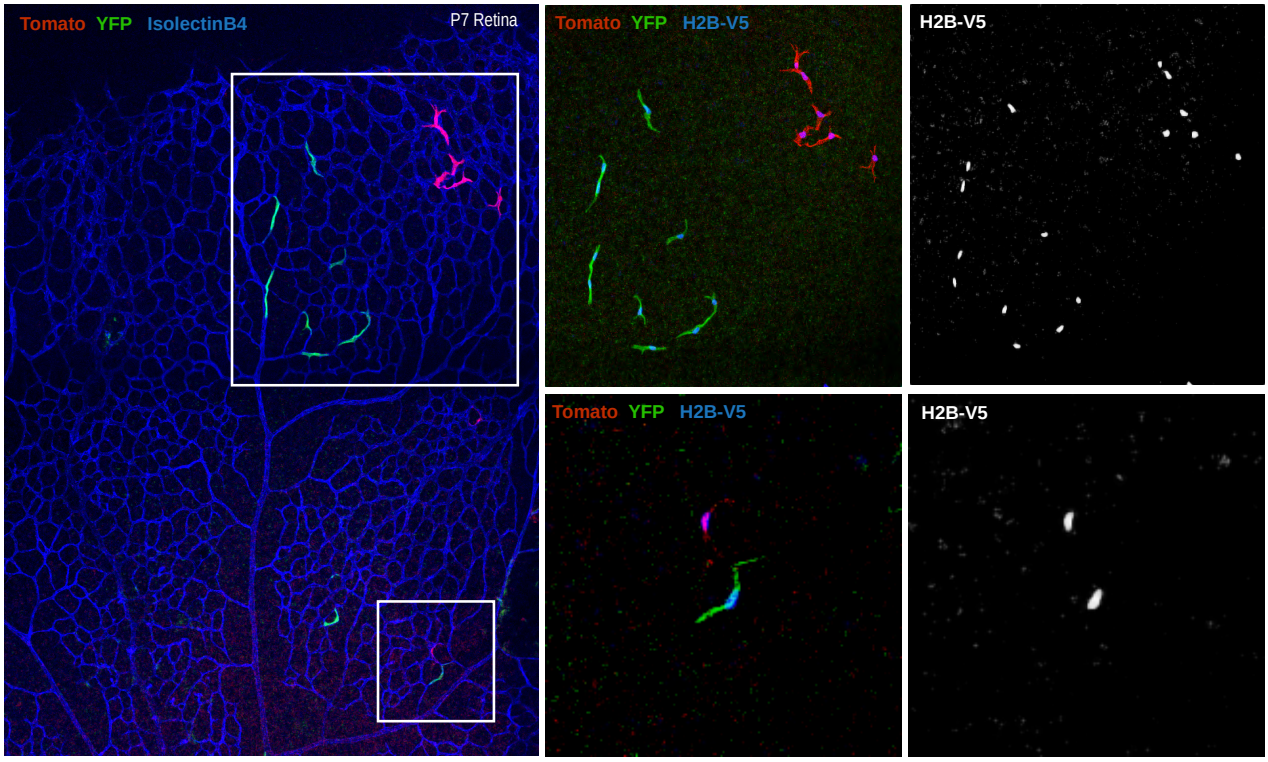

Supplementary Figure 7

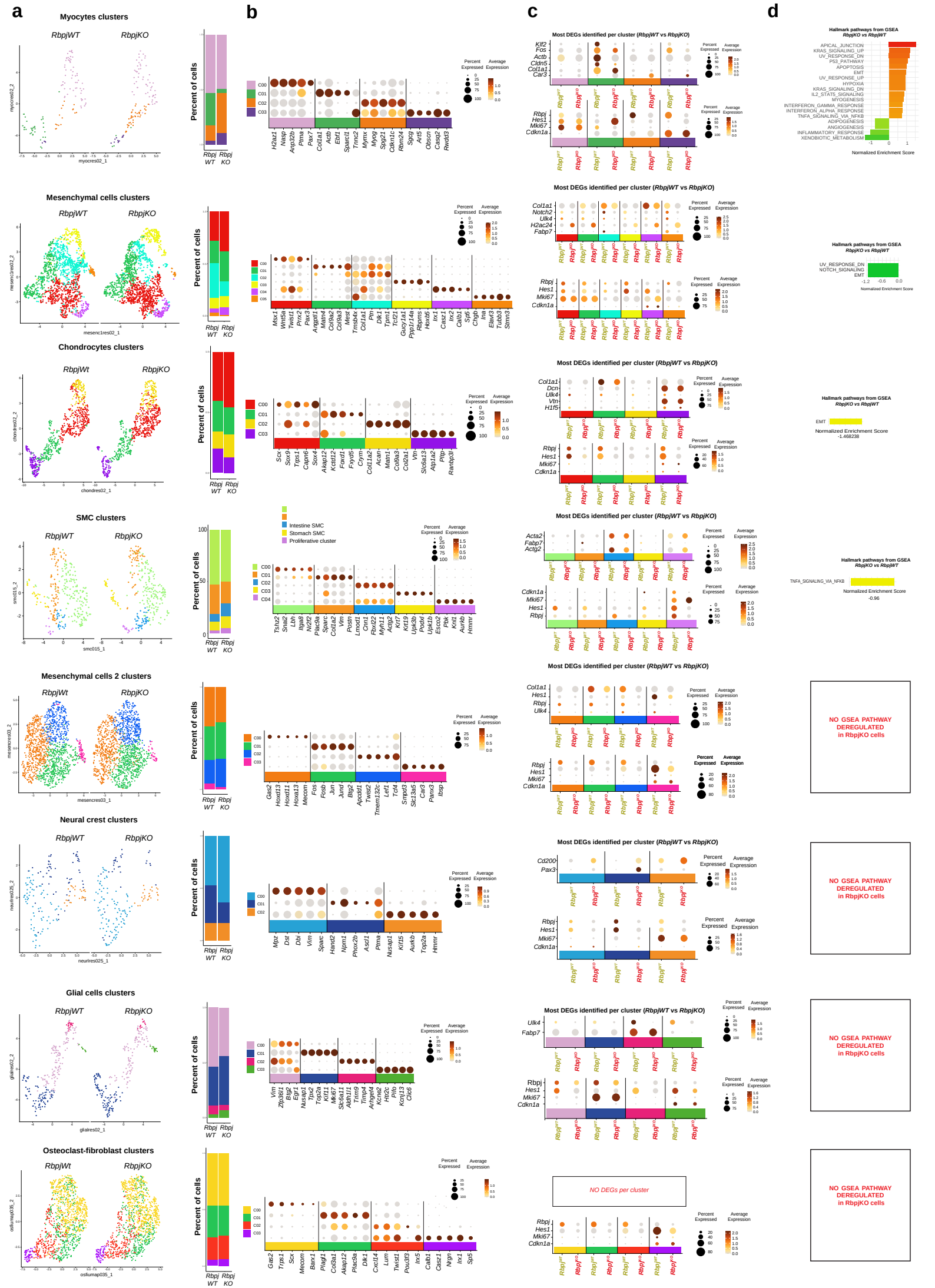

Supplementary Table 1

Ref		Mouse line	Band size	Genotyping primers
Generated in this study	iFlp-Mosaics	*Gt(ROSA)26Sor-iFlpMbTomato-2A-cre/MbYFP*	WT: 250bp KI: 380bp	QPCR MAN YFP F II CTGCCCGACAACCACTACCT RR713 CTTTAAGCCTGCCCAGAAGA WPRE REV GTTGCGTCAGCAAACACAGT RR711 GCACTTGCTCTCCCAAAGTC
		Tg(ROSA)26Sor-iFlpMbTomato-2A-H2B-GFP2A-cre/MbYFP2A-H2B-Cherry-2A-Flpo	TG: 369bp	GFP SEQ F: CGACAACCACTACCTGAGCA CREM R: TCCCTGAACATGTCCATCAG
		Tg(ROSA)26Sor-iFlpChromatin	TG: 300bp	FRT1 DUM F TGTTGTTGAAGCTTGAAGTTCCT CHERRY DUM R GCTCGAAAATGTCGTTCACA
	FlpOERT2	*Tg(Cdh5(PAC)-FlpoERT2)*	TG: 538bp	CDH5 TRANS F: GGAGGCTGGAAAGTAGAGCA FLPO TRANS AND SEQ REV: GTCTTGCACAGGATGTCGAA
		Tg(INS-CAG-FlpoERT2)	TG: 530bp	FLPOERT2 F GENOTYPING GCCCTGGTGTCCAGGTACTA FLPOERT2 R GENOTYPING AGGATCTCTAGCCAGGCACA
	DreERT2	*Tg(INS-CAG-DreERT2)*	TG: 249bp	CAG F: GCAACGTGCTGGTTATTGTG Dre R II: CTAGCGTGGCACCATCTAGC
	FlpO and dre Inducible	*Tg(iFlp/Dre ^{iProgenitor})*	TG: 412bp	AR124 1A HCD2 SEQ: TGAATGGAACTGACCCCGAA NCOI-FLPO R: GTCTTGCACAGGATGTCGAA
Ref		**Mouse line**	**Band size**	**Genotyping primers**
(Lao, Raju, Bai, & Joyner, 2012)	FlpO drivers	*Gt(ROSA)26SorCAG-FlpoERT2*	WT:630bp KI: 309bp	FLPO/ERT2 MUT TTA TGT AAC GCG GAA CTC CA FLPO/ERT2 COM AAA GTC GCT CTG AGT TGT TAT FLPO/ERT2 WT GGA GCG GGA GAA ATG GAT ATG
(Luo et al, 2021)		*Apln-Flpo*	KI: 292bp	HA F CATGGCGTATCCATATGACG FLPO REV GTTCACGATGTCGAAGCTCA
(Farley et al., 2000)		*Gt(ROSA)26Sortm1(FLP1)*	KI: 260bp	FLPES CTAATGTTGTGGGAAATTGGAGC FLPEAS
(de Alboran et al, 2001),	Floxed	*Myc ^{flox}*	WT:315BP MUT: 370BP	MYC FLOX RB F GACAGGGATGTGACCGATTC MYC FLOX RB R GCTCAGTCTCCGGCTATCAC
Paik et al., 2007		*Foxos1 ^{flox}*	FLOX 149 BP WT: 115	FOXO 1 PRIMER A: GCTTAGAGCAGAGATGTTCTCACATT FOXO 1 PRIMER B: CCAGAGTCTTTGTATCAGGCAAATAA FOXO 1 PRIMER D: CAAGTCCATTAATTCAGCACATTGA
Paik et al., 2007		*Foxos3 ^{flox}*	FLOX: 138 WT 100	FOXO 3 PRIMER A: ATTCCTTTGGAAATCAACAAAACT FOXO 3 PRIMER B: TGCTTTGATACTATTCCACAAACCC FOXO 3 PRIMER D: AGATTTATGTTCCCACTTGCTTCCT
Paik et al., 2007		*Foxos4 ^{flox}*	FLOX 555 WT: 343	FOXO 4 PRIMER A: CTTCTCTGTGGGAATAAATGTTTGG FOXO 4 PRIMER B: CTACTTCAAGGACAAGGGTGACAG FOXO 4 PRIMER D: TGAGAAGCCATTGAAGATCAGA
(Han et al, 2002)		*Rbpj ^{flox}*	WT:200bp Flox:350bp	RBPJLOX F ATAATTTGCCAAGCCAAAGC RBPJLOX R GCTCCCCACTGTTGTGAACT
(Srinivas et al, 2001)	Reporter	*Gt(ROSA)26LSL-EYFP*	WT: 250bp KI: 350bp	RR711 GCACTTGCTCTCCCAAAGTC RR713 CTTTAAGCCTGCCCAGAAGA CAG PCR F CGGGGTCATTAGTTCATAGCC CAG PCR R CACCTCGACCATGGTAATAGC
(Madisen et al, 2010)		*Gt(ROSA)26LSL-tdTomato*		
(Pontes-Quero et al., 2017)		*Tg(Rosa)26Sor(iMb2-Control-Mosaic)*	TG: 600bp	LOXP3 SEQ F: TCAATGTATCTTAAGGCGTGACT MTFP1 R: TACTTGGTGAAGGCCCTGTT
		Gt(Rosa)26Sortm1(iChr-Control-Mosaic)	TG: 550bp	CTP PHI F ACGTGAAGCTGAGCAAGGAT CTP H2B R CTTAGTCACCGCCTTCTTGG
(Wang et al, 2010),	Cre drivers	*Tg(Cdh5-CreERT2)*	TG: 600bp	CDH5 TRANS F GGAGGCTGGAAAGTAGAGCA CREM R TCCCTGAACATGTCCATCAG
(Fernandez-Chacon et al, 2019)		*Tg(iSuRe-Cre)*	TG: 350bp	CREM R QPCR MAN MTOMATO F II CCGCTACCTGGTGGAGTTCA

Supplementary Table 2

Antibody	Dilution	Source	Reference
Primary Antibodies			
Biotinilated Isolectin B4	1:100 (IF)	VECTOR LABS	B-1205
Rat anti- mouse p21 Rat monoclonal Clone: HUGO291 Supernatant	1:50 (IF)	CNIO	#
Monoclonal Rabbit anti-ERG [EPR3863]	1:500 (IF)	ABCAM	Ab110639
Goat Polyclonal Anti-GFP and YFP/CFP variants	1:200 (IF)	Acris	R1091P
Anti-PECAM-1 Antibody, clone 2H8 hamster anti mouse CD31	1:200 (IF)	Merck	MAB1398Z
Rabbit anti- DsRed (Living colors)	1:200 (IF)	Clontech	632496
Rabbit anti-RFP/Dsred/Tomato/Cherry CF543 conjugated (Polyclonal)	1:200 (IF)	Biotium	20476
Mouse anti HA-Tag (6E2) Mouse mAb (Alexa Fluor® 647 Conjugate)	1:200 (IF)	Cell Signaling	3444
RABBIT ANTI-RFP/Dsred ConjugatedCF594	1:200 (IF & FC)	Sigma or Biotium	BTIU20422
Rabbit Anti-ERG Alexa Fluor® 647 EPR3864	1:500 (IF)	ABCAM	ab196149
Rat anti-Ki-67 Monoclonal Antibody (SolA15), eFluor 660, eBioscience™	1:250 (IF)	Thermo Fisher Scientific	50-5698-82
APC Rat Anti-Mouse CD31	1:250 (FC)	BD Bioscience	551262
APC-Cyanine7 Rat Anti-Mouse CD45.2	1:250 (FC)	TonboBio	25-0454-U025
Mouse anti HA-Tag (6E2) Mouse mAb (Alexa Fluor® 647 Conjugate)	1:250 (IF)	Cell Signaling	3444
BV711 Rat Anti-Mouse CD31 Clone MEC 13.3 (RUO)	1:250 (FC)	BD Biosciences	740680
Rabbit anti GFP Conj. Alexa-488	1:200 (IF & FC)	Invitrogen	A213111
BD Horizon™ BV605 Rat Anti-Mouse CD45	1:200 (FC)	BD Biosciences	563053
Anti-Mouse CD150 (SLAM) Antibody Brilliant Violet 510™	1:300 (FC)	Biolegend	115929
Anti-Mouse CD48 APC Cy7	1:100 (FC)	Biolegend	103432
Anti-Mouse CD117 (c-kit) PercP Cy5.5	1:200 (FC)	Biolegend	105824
Anti-Mouse Ly-6A/E (Sca-1) FITC	1:200 (FC)	eBioscience	11-5981-85
Biotin Mouse Lineage Depletion Cocktail	1:200 (FC)	BD Biosciences	51-9000794
Secondary Antibodies			
Streptavidin, Alexa Fluor® 405 conjugate	1:200 (IF)	Thermo Fisher Scientific	ST32351
Donkey Anti-Rat IgG H&L (Alexa Fluor® 647) preadsorbed	1:400 (IF)	ABCAM	ab150155
Cy™3 AffiniPure Fab Fragment Donkey Anti-Rabbit IgG (H+L)	1:400 (IF)	Jackson	711-167-003
AffiniPure Goat Anti-Armenian Hamster Alexa680	1:400 (IF)	Jackson	127-625-16

Supplementary Table 3

Taqman Assays

Gene Symbol	Dye	Assay ID	Source
Rbpj	FAM-MGB	Mm01217627_g1	Thermo Fisher
Myc	FAM-MGB	Mm00487804_m1	Thermo Fisher
Mycn	FAM-MGB	Mm00476449_m1	Thermo Fisher
Notch1	FAM-MGB	Mm00435245_m1	Thermo Fisher
Pecam1	FAM-MGB	Mm01242584_m1	Thermo Fisher
Gapdh	FAM-MGB	Mm99999915_g1	Thermo Fisher